School of Chemistry

Fabrication of Diamond-Coated Wires for Fibre Reinforced Polymers

Isabelle Hone

This thesis is submitted in partial fulfilment of the requirements for the Honours Degree of MSci Chemical Physics at the University of Bristol

Supervisor: Professor Paul May

Second Assessor: Professor Neil Fox

Physical and Theoretical Chemistry

Statement of factors which limited project progress

The modifications of the Thomas Swan reactor took much longer than expected, which consequently delayed the progress of the overall project. The conversion of the reactor depended on multiple external factors, and therefore, delays in the ordering of parts, long production times for custom-made parts from the workshop and plumbing issues requiring specialised assistance all contributed to the overall setback. As a result, the Thomas Swan was only operational very late into the project, specifically only a few days before the allocated laboratory time ended, which did not allow time for optimising conditions of the growth, an overnight run, or more than two runs.

Additionally, there were logistical limitations that impacted the resin compatibility testing that took place at the National Composite Centre. Resin bonding was originally planned, but unavailability of extraction booths within the time frame and delays in approval of COSHH forms and BPS checks led to this being prevented. Consequently, the resins used were commercially available instead.

These limitations, in addition to the HFCVD reactor being out of use for approximately 4 weeks due to maintenance in the laboratory, contributed to slower progress throughout the project than anticipated.

Abstract

Fibre reinforced polymers (FRPs) are widely utilised in a range of sectors, including aerospace, automotive, defence and infrastructure. However, the compromises made between mechanical performance, thermal conductivity and environmental sustainability motivate the investigation of alternative, high-performance reinforcement materials. Diamond exhibits an exceptional combination of properties, including extreme hardness, high stiffness and very high thermal conductivity. By fabricating diamond-coated wires, namely diamond fibres, it is possible to harness these remarkable properties, presenting an ideal high-performance fibre material.

The primary aim of this thesis was to modify and repurpose the Thomas Swan reactor to enable the fabrication of diamond-coated tungsten wires via hot filament chemical vapour deposition (HFCVD), and in turn, establish a reliable method for their production. To provide a comparison, a conventional hot filament reactor was utilised to deposit diamond coating onto 100 µm tungsten wires. Laser Raman spectroscopy confirmed the presence of high purity diamond with a characteristic peak at 1332 cm^{-1}. However, Scanning Electron Microscopy (SEM) imagery revealed that the growth was relatively non-uniform across the wire substrates, likely due to the unfavourable geometry of the wire in the reactor.

Preliminary adhesion testing was conducted using a PosiTest AT-A pull-off tester to evaluate the interfacial bonding between the CVD diamond surface and bisphenol A epoxy resins. To provide a suitable, planar surface for this, diamond was deposited onto 10 x 10 mm silicon wafers using a conventional hot filament reactor. Results demonstrated measurable adhesion with a commercially available Bisphenol A resin containing a silane coupling agent, which recorded a pull-off force up to 66 N.

Two trial runs in the Thomas Swan reactor were carried out: a singular 8-hour growth and a 20-hour growth carried out in three cycles. Diamond films were successfully deposited on the tungsten wires during both runs; however, Raman spectroscopy identified a high sp^2 carbon content present. This was further confirmed by SEM imagery, which illustrated early-stage nucleation and incomplete film deposition. Despite the longer total growth time, the three-cycle growth method resulted in reduced diamond quality, indicating that this method is ineffective for maintaining high-purity diamond quality. In both cases, the conditions were not exhaustively optimised, so further optimisation of the Thomas Swan reactor conditions is required to achieve thicker, high-quality growth for effective implementation of diamond FRPs.

Acknowledgements

Firstly, I would like to express my sincere gratitude to Professor Paul May for his guidance and support throughout this project, particularly for his advice and feedback during my thesis writing. I would also like to thank Professor Neil Fox, for his support during meetings, and for helping me come up with alternate ideas for my project in the periods when progress with the Thomas Swan reactor was slow. I am also grateful for his support throughout the four years of my degree as a chemical physicist.

Thank you to James Swarbrigg for his supervision in the lab and for his advice throughout the project, particularly during my presentation preparation and the writing of my thesis. I would also like to thank Dr James Smith for his assistance with the Thomas Swan modifications and for always being willing to offer help and answer questions. Also, to Dr. Ed Smith for his help with the plumbing of the Thomas Swan reactor.

I would like to acknowledge the whole of the BUDGie group for their encouragement and assistance throughout the duration of this project. It has been a pleasure to work in such a welcoming environment.

Finally, I am grateful to my friends and family for their encouragement, and especially to my parents for their invaluable support.

Table of Contents

List of Figures

List of Tables

List of Abbreviations

AFRP - Aramid Fibre Reinforced Polymer
CFRP - Carbon Fibre Reinforced Polymer
CH_4 - Methane
Cu - Copper
CVD - Chemical Vapour Deposition
FRP - Fibre Reinforced Polymer
GFRP - Glass Fibre Reinforced Polymer
H_2 - Hydrogen
HF - Hot Filament
HFCVD - Hot Filament Chemical Vapour Deposition
HTHP - High Temperature High Pressure
IPA - Isopropanol
LEXT - Laser Microscope (Olympus LEXT system)
MWCVD - Microwave Plasma Chemical Vapour Deposition
NCC - National Composite Centre
NFRP - Natural Fibre Reinforced Polymer
PAN - Polyacrylonitrile
PE - Polyethylene
PEEK - Polyetheretherketone

PEK - Polyether ketone
PET - Polyethylene terephthalate
PHA - Polyhydroxyalkanoate
PLA - Polylactic Acid
PP - Polypropylene
PTFE - Polytetrafluoroethylene
RTM - Resin Transfer Moulding
SEM - Scanning Electron Microscopy
Si - Silicon
SiC - Silicon carbide
Ti - Titanium
TiC - Titanium carbide
$\mathbf{T_g}$ - Glass Transition Temperature
VARTM - Vacuum-Assisted Resin Transfer Moulding
W - Tungsten

1. Introduction

1.1 Fibre-Reinforced Polymer Composites

The concept of using composite materials stretches back thousands of years, where mud bricks were embedded with grass and straw during the creation of the first shelters to provide stronger structural support.[1] A composite material consists of two or more different materials, each with distinct individual properties, combined to create a resulting material with new, enhanced properties.[2]

Fibre-reinforced polymers (FRPs) are an essential type of composite material, made up of a polymer matrix embedded with multiple fibres to provide reinforcement to the material, as illustrated in Figure 1.1. The fibres act as the load-bearing element of the composite and the matrix material binds the fibres together, keeping them protected and ensuring the load can be transferred between each of the fibres.[3] Fibre reinforcement can be considered a complementary modification to a polymer material, for example, most commonly allowing a material to remain lightweight, whilst exhibiting substantially improved strength and/or stiffness. In composite materials, strength is defined as the resistance to fracture, while stiffness is the resistance to deformation, associated with Young's modulus of elasticity.[2]

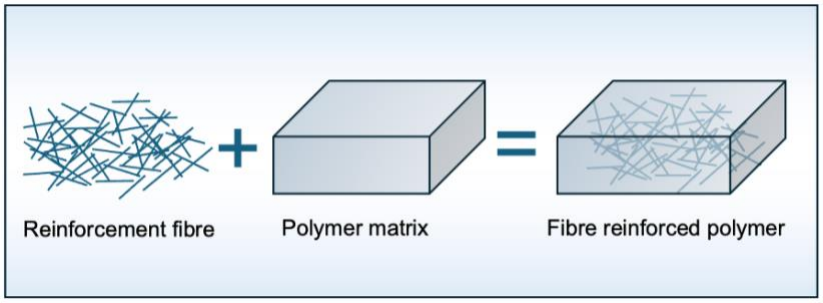

Figure 1.1: An illustration of how the reinforcement fibres are implemented into the polymer matrix to create a fibre reinforced polymer. Reproduced with reference to[4].

The development of FRPs originated in the 1900s, but became commercially recognised in the 1940s with the emergence of glass-fibre-reinforced polymers in military and automotive industries.[5, 6] The evolution of FRPs continued with the advancement of carbon-fibre-reinforced polymers in the 1960s, followed by aramid-fibre-reinforced polymers in the 1970s.[5]

Over the last few decades, the widespread use of FRPs to replace metals or ceramics has become common practice, due to their excellent strength-to-weight ratio, resistance to corrosion, and flexibility, in addition to improved cost-effectiveness.[7] FRPs exhibit an exhaustive list of properties making them appealing for many applications, from aerospace and automotive sectors to construction and defence. The desired characteristics of FRPs can be tailored depending on

multiple factors during the manufacturing of FRPs, such as the raw materials (i.e. fibre and matrix) chosen, the orientation in which the fibres are arranged, the interfacial bonding between the fibre and matrix and the manufacturing process undertaken.[7] More recently, research within this area has targeted the effects of including nanoparticles, such as carbon nanotubes, as fillers and including flame-retardant and UV- or high temperature-stabilising additives, to create highly specific properties.[8-10]

Despite their use in a range of applications, FRPs remain limited by compromises made in mechanical properties, thermal conductivity, corrosion resistance and environmental sustainability, motivating the exploration of new and alternative reinforcement materials.

1.2 Fibres in Reinforcement

Fibres primarily act as a load-bearing framework in most composites, possessing a multitude of beneficial mechanical properties specific to the material chosen. Depending on their composition, fibres can be categorised into natural or synthetic fibres (Figure 1.2).

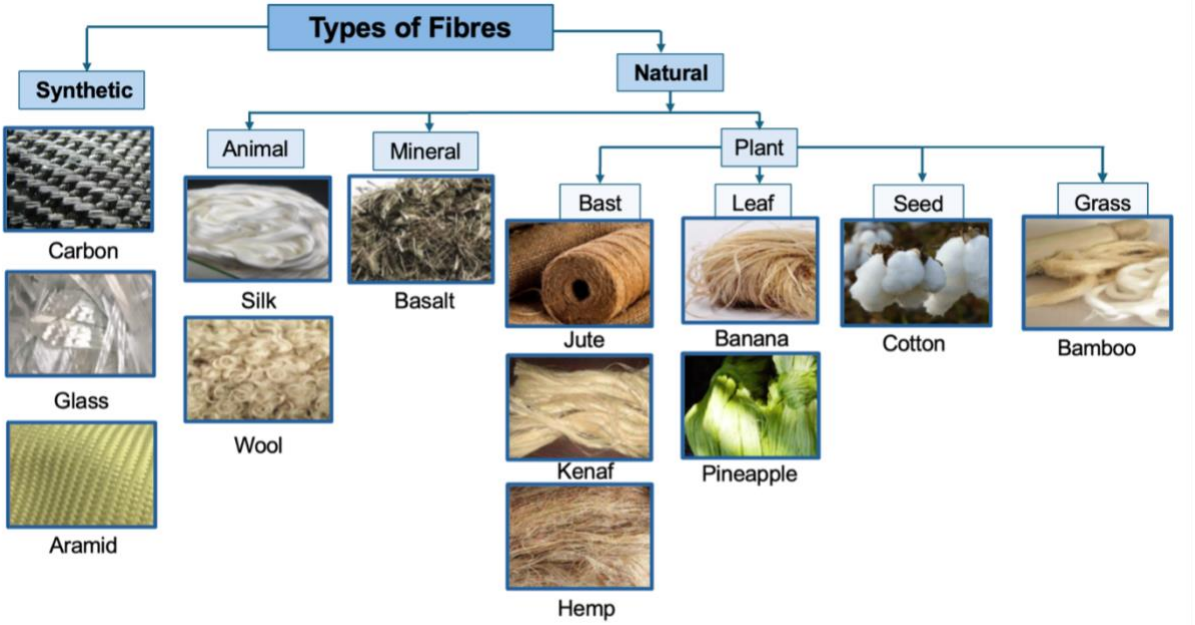

Figure 1.2: A flow chart depicting how fibres are categorised into natural and synthetic fibres. Natural fibres are then further divided into animal, mineral and plant. An example image is provided for each category. Photos taken from[11-14]. Flow chart adapted from[11].

1.2.1 Synthetic Fibres

Synthetic fibres are artificially produced through chemical processes. They can be categorised into organic fibres, such as aramid or polyethylene, and inorganic fibres, such as carbon or glass.[15, 16] These fibres benefit from a higher resistance to strain or corrosion, exceptional tensile strength and excellent durability when compared to natural fibres, resulting in synthetic fibres being the most commonly used fibres for the production of FRPs.[7, 15] Despite this, the environmental downfalls of synthetic fibres, such as the inability to biodegrade and the environmental costs of the manufacturing processes, remain a concern. Furthermore, current research stresses the necessity for proper waste management and recycling of fibres and FRPs.[7, 17-19]

1.2.1.1 Glass Fibres for Glass-Fibre Reinforced Polymers (GFRPs)

GFRPs, frequently termed 'fibreglass', have been developing rapidly since Dale Kleist's accidental discovery of glass fibres in the 1930s, and are still ubiquitous today.[5] They consist of glass threads embedded into a polymer matrix to create a lightweight, high-strength composite material. Although, independently, glass fibres can shatter easily when bent, the polymer acts to support the glass threads and distribute the load between them.

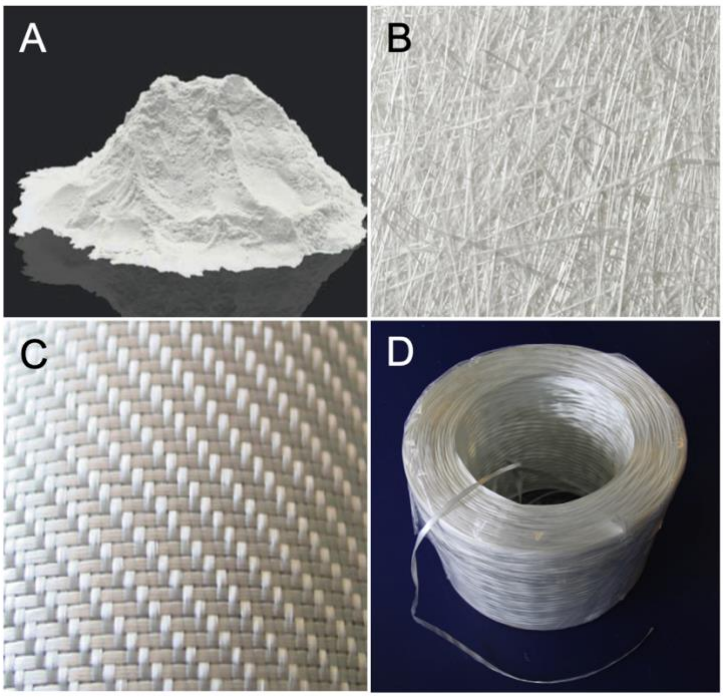

Figure 1.3: The different forms of glass fibre. A) In a powdered form (milled fibres). B) Chopped strand mat. C) Woven mat. D) Continous fibre roving. Photos taken from[20, 21]

Currently, GFRPs are the predominant choice for FRPs in industry, constituting over 90% of the global FRP market, due to the balance of their versatile, high-performance properties with cost-

effectiveness relative to other FRPs.[22]. Literature consistently reports that GFRPs offer excellent tensile strength, high corrosion resistance and great strength-to-weight ratio, often at a significantly lower cost than carbon or aramid based FRPs.[23-26] The glass fibres used in GFRPs are manufactured from abundant raw materials, contributing to their cost-effectiveness and global accessibility.[27] Within the infrastructure sector, GFRPs provide an appealing alternative to steel, particularly in aggressive environments where their resistance to moisture and chemical degradation extend service life. GFRPs boast tensile strength values comparable to steel, at a considerably lower density.[28] Additionally, as GFRPs can be both electrical insulators and non-magnetic, they can be implemented in unique environments where other material reinforcements may cause electromagnetic interference, such as in electronic devices or high-voltage power systems.[29, 30]

Table 1: The different classifications of glass fibres and their properties, adapted from [27, 28, 31, 32].

Classification	Composition	Tensile Strength / MPa)	Young's Modulus / GPa	Properties
A Glass	Alkali-lime with no or low levels of boron oxide present	3.30	69.0	High durability, strength and electrical resistivity
AR Glass	Silica-based with zirconium oxide or zirconia	3.24	73.1	Alkali resistant
C Glass	Alkali-lime with high levels of boron oxide	3.32	68.9	High chemical corrosion resistance (i.e. to acid and chemicals)
D Glass	Borosilicate glass	2.42	51.7	Low dielectric constant
E Glass	Alumino-borosilicate glass with no alkali present	3.45	72.31	All- purpose, high strength and electrical resistivity
R Glass	Alumino-silicate glass with no CaO and no MgO present	4.13	85.58	High mechanical properties and corrosion resistance, predominantly for reinforcement
S Glass	Alumino-silicate glass with no CaO but high levels of MgO	4.88	86.92	Highest tensile strength and high heat resistance.

Due to their brittle nature, isolated glass fibres exhibit low fracture toughness. Consequently, if a crack arises, the stress at this point is significantly amplified and there is no mechanism in place to prevent or even slow its propagation.[23] The addition of a polymer matrix fundamentally alters this property; the new fibre-matrix interface provides energy-dissipative mechanisms in the

presence of a crack (such as crack deflection and interfacial debonding), resulting in a glass-polymer composite characterised by high toughness.[23] Glass fibres can be classified and given code labels depending on their chemical composition and/or potential applications, as displayed in Table 1.[27, 33] For example, E-glass is a popular, cost-effective choice for GFRPs, S-glass is a good choice for when tensile strength needs to be prioritised and C-glass is ideal for applications in a corrosive environment.[7] Glass fibres can be produced in various forms including chopped strand mats (randomly oriented chopped fibres held together), woven mats, and even powder, as displayed in Figure 1.3.[27] Frequently, glass fibres are paired with a thermoset polymer, such as polyester or epoxy.[34]

However, it is important to note the relatively low elastic modulus and fatigue resistance of GFRPs when compared to reinforced polymers using carbon fibres, motivating the continued exploration of alternative high-performance and hybrid reinforcement strategies.[28]

1.2.1.2 Carbon Fibres for Carbon Fibre Reinforced Polymers (CFRPs)

Production of carbon fibres dates back as far as the 1800s for their use in lightbulb manufacturing, but the re-introduction of carbon fibres with increased mechanical properties began in the late 1950s.[5]

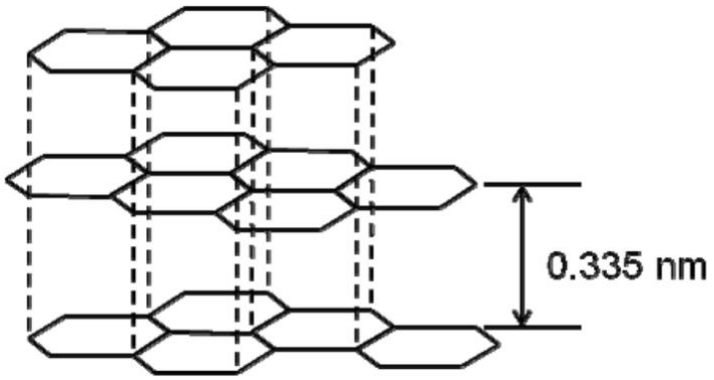

Figure 1.4: The structure of graphene, displaying a stacked, layer formation. Taken from[35].

Carbon fibres have the same crystalline structure as graphene, composed of stacked layers of hexagonally arranged carbon atoms, as depicted in Figure 1.4.[36] Within the plane of these rings, the carbon atoms are covalently bonded via overlap of strong sp^2 hybridised orbitals resulting in high tensile strength, while the presence of delocalised π electrons contribute to high electrical conductivity.[35] However, the carbon layers themselves interact through weak van der Waals forces. The carbon layers lie parallel to the fibre axis, resulting in anisotropic character, where the modulus of elasticity, thermal conductivity and electrical conductivity are higher along the direction of the fibre than in the transverse direction.[36] The precursor chosen and manufacturing process conditions used determine whether the structure of the layer planes is predominantly turbostratic, graphitic or a hybrid of both. In graphitic regions, the layers are aligned in an

ordered, parallel stacking arrangement, whereas in turbostratic regions, the graphene sheets are stacked irregularly with slightly larger interlayer spacing.[35]

90% of carbon fibres are manufactured with polyacrylonitrile (PAN) as the precursor, with the other 10% consisting of fibres produced from petroleum pitch or rayon.[7] In both PAN-based and pitch-based carbon fibres, the graphene sheets are oriented parallel to the fibre axis.[7, 35] However, PAN-based carbon fibres offer higher tensile properties due to the smaller size of their π-orbital-oriented domains and shorter graphene stack height, unlike the larger crystalline structure of pitch-based fibres.[35, 37] Therefore, PAN-based carbon fibres are favoured for high strength applications, while pitch-based carbon fibres are preferred when high stiffness or thermal conductivity is of priority but a lower strain is permissible.

Although the processing conditions will vary with the precursor chosen, the basic manufacturing process for most precursor materials is similar and follows a sequence of heating and tensioning steps.[35] Typically, this begins with spinning of the precursor, followed by oxidative stabilisation and high-temperature carbonisation to remove non-carbon elements.[35] To improve the fibre-matrix adhesion, surface treatment and sizing normally takes place.[7, 38]

Table 2: Carbon fibres categorised based on physical properties adapted from[35].

Tensile Modulus Category	Elastic Modulus / GPa
Ultra-High Modulus	>500
High Modulus	350 - 450
Intermediate Modulus	200 - 350
Low Modulus	>100
High Strength	>4

Carbon fibres possess an exhaustive list of advantageous properties: very high strength-to-weight ratio, exceptional tensile strength, high thermal and electrical conductivities, excellent temperature and chemical resistance, low density. There is not a single standardised method to categorise carbon fibres. While it is common to categorise by precursor material, they are more often classified by physical properties, such as their tensile modulus seen in Table 2, as they are often purchased this way.

The resulting composite of carbon fibres embedded in a polymer matrix leads to a highly durable composite with an exceptional stiffness and strength-to-weight ratio.[39] In applications where the mechanical properties of a material are of higher priority than the cost effectiveness, CFRP is the

standard choice. Despite a higher manufacturing cost, CFRP is widely implemented across a wide range of industries including aerospace, defence, construction and automotive sectors. For example, CFRP constitutes 50% of the Boeing 787 Dreamliner's structure by mass as depicted in Figure 1.5.[40]

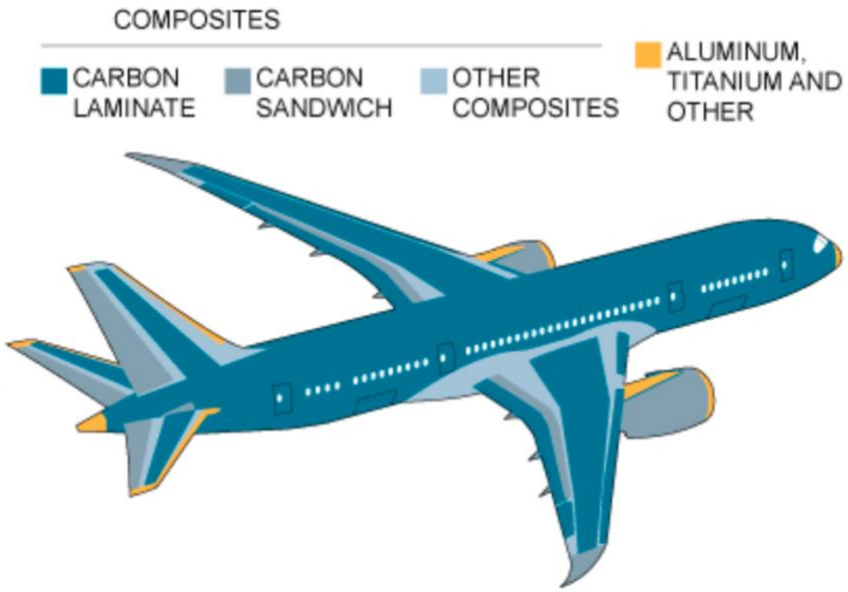

Figure 1.5: An illustration of the Boeing 787 Dreamliner, highlighting the parts made up of carbon composite materials. Taken from[40].

As CFRPs are characterised by their excellent strength-to-weight ratio, they are particularly useful in weight-conscious applications such as in bridges, tall buildings or aircrafts, especially in comparison to generic construction materials such as steel or concrete.[41] Table 3 illustrates significant properties of CFRP in comparison to alternatives, GFRP and steel. The high fatigue resistance and resistance to corrosion in chemical or aggressive environments leads to a longer service life, making them technically more cost-effective in the long term, if the initial budget allows. Nevertheless, the high initial cost of CFRP in comparison with conventional building materials, makes them unattainable for some projects, and this issue stands as a primary restriction in the wide-spread implementation of CFRP in the construction industry.[41] However, if the initial expense can be met, the durability and long service life of CFRP, especially in aggressive environments, is a cost-effective choice for the long term in comparison with steel or concrete. Additionally, efforts have been made to develop methods to reduce the manufacturing cost of carbon fibres, for example investigating alternative precursors, such as lignin, or combining PAN with bio-based polymers or recycled plastic waste.[42, 43]

Table 3: Mechanical properties of CFRP in comparison to GFRP and steel. Note the large variation in the CFRP values is due to the different strength or modulus values possible for carbon fibres (as seen in Table 2). Table made with reference to[28].

Material	Tensile Strength / MPa	Young's Modulus / GPa	Density / (gm cm^{-3})
CFRP	~ 600–3900	~ 40–780	1.50–2.10
GFRP	~ 480–4580	35–86	1.25–2.50
Steel	~ 480–690	200	7.85

A further challenge is that, although carbon fibres exhibit exceptional mechanical properties in the lateral direction of the fibre axis, the low compressive strength and anisotropic nature of carbon fibres can lead to engineering constraints.[28] Mechanical performance is significantly influenced by the fibre orientation and composite design, which can impose limitations for structure applications.[31] In addition, their graphitic structure causes carbon fibres to be extremely brittle, leading to more extensive and costly manufacturing processes.[39]

While the chemical inertness of carbon fibre makes it highly resistant to corrosion, it can also result in poor adhesion with the matrix. As previously emphasised, the interface between the fibre and matrix impacts the resulting mechanical properties of the composite.[44] Increasing the surface roughness and wettability of the carbon fibres has been found to improve the interfacial adhesion and ultimately enhance the mechanical properties. Sizing, a process whereby a thin coating of polymer can be applied to the fibre surface, has been reported to increase fibre-matrix adhesion, but is heavily dependent on the chemical and surface properties of both the fibre and matrix.[45, 46] Additionally, other chemical treatments can improve surface roughness of the fibres, such as acidic treatments that improve interlocking system of the fibre-matrix[47], or more commonly, electrochemical oxidation, which uses an oxidative potential to etch the surface of the fibre.[48] Physical treatments can also be implemented: plasma treatments that expose the surface to high-energy electrons and ions to modify surface properties, and radiation treatments that enhance chemical bonding by introducing reactive functional groups and increasing surface roughness through, for example, microwaves or gamma rays.[49, 50]

1.2.1.3 Aramid Fibres for Aramid Reinforced Polymers (AFRPs)

Aramid fibres are an organic type of synthetic fibres composed of aromatic polyamide chains. The US Federal Trade Commission formally accepted the shortening of "aromatic polyamide" to "aramid" in 1974, defining an 'aramid fibre' based on the criteria that in a long-chain polyamide at least 85% of the amide bonds are directly attached to two aromatic rings.[51]

Aramid possesses a unique combination of thermal, mechanical and chemical properties which come together to produce a highly valued, multifaceted fibre-reinforced polymer, rather than excelling in just one property.[52] Most notably, aramid fibres exhibit an exceptionally high strength-to-weight ratio, excellent chemical resistance and useful non-conductive properties, in addition to being entirely heat and flame resistant.[7, 51, 53] The combination of aramid's properties means that AFRPs are most frequently used in areas such as the defence sector or aerospace industry, where impact resistance or thermal stability is a priority, rather than solely prioritising high stiffness.[16, 52] AFRP is utilised within the defence industry for helmets and body armour (Figure 1.6) to provide a lightweight, durable alternative material that does not restrict mobility, compared to previously used metallic armour.[16]

Figure 1.6: Aramid FRP bulletproof vest and helmet for defence purposes. Images from[16]

These attractive properties of aramid are a consequence of its polymeric structure and aromatic features. The molecular structure of aramid follows a pattern of repeating benzene rings linked by amide groups to form long, highly ordered polymer chains.[51] Aramids can be divided into *para*-aramids and *meta*-aramids dependent on the position of the amide bonds on the benzene rings, as displayed in Figure 1.7. The properties, and therefore applications, vary for both the *meta*- and *para*-aramid configurations.

Aramid was introduced commercially by DuPont with the *meta*-aramid fibre, Nomex, in 1967.[51] Due to its nonconductive properties, its arrival was very successful in thermal and electrical insulation industries.[5] The development of the more commonly known *para*-aramid fibre, Kevlar, followed in the early 1970s, when it emerged on the market as a new high-tensile-strength fibre and a less brittle alternative to carbon or glass fibre.[5]

Para-aramid is composed of linear polymer chains, resulting in very stiff molecular structure. Strong intermolecular hydrogen bonds can form between adjacent chains to form a highly ordered structure with extremely high tensile strength, resulting in *para*-aramids being characterised by their mechanical performance and use in protective and structural applications.[54] The nature of the covalent bonding along the *para*-aramid fibres makes it anisotropic, with a

higher strength along the direction of the fibres, but with weak transverse properties and low compressive strength.[51]

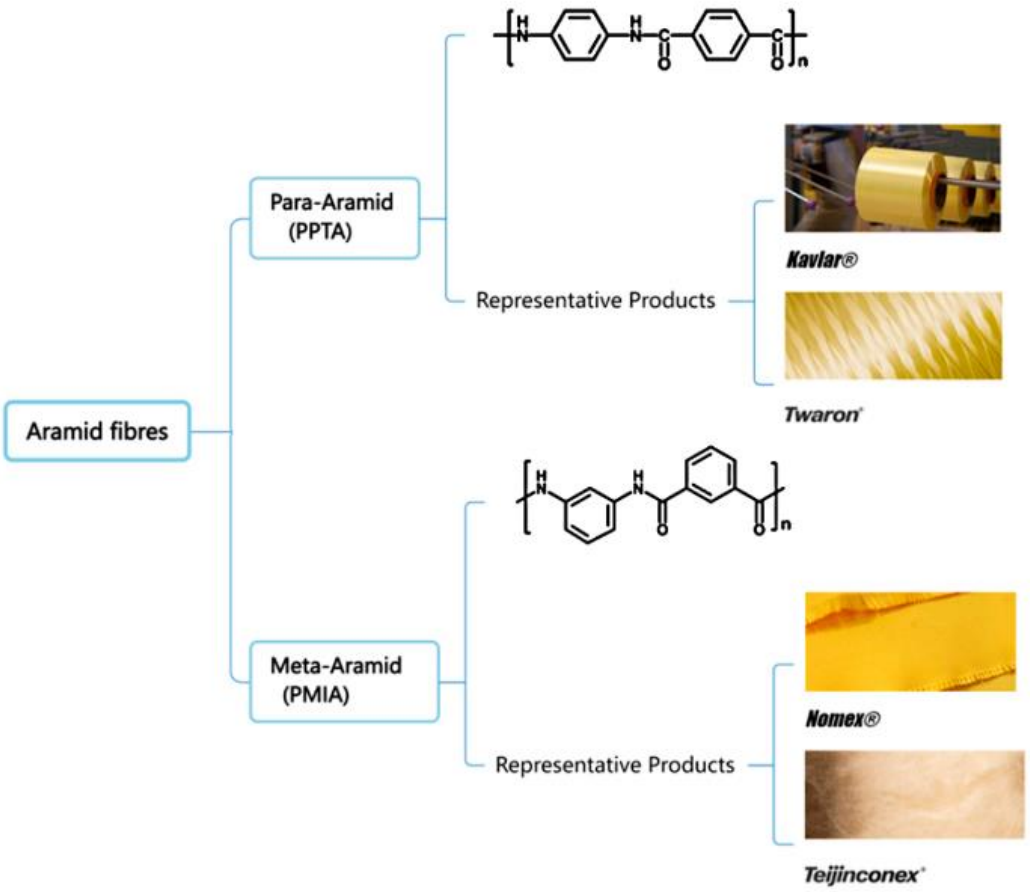

Figure 1.7: The *para*- and *meta*-aramid structures and their respective representative products. Adapted from[52].

In contrast, *meta*-aramids exhibit a non-linear "zig zag" configuration, reducing alignment between neighbouring chains and leading to lower tensile strength.[51] The *meta*-aramid structure instead provides exceptional thermal and flame resistance, withstanding short-term exposure to temperatures above 300 °C, leading to their use in situations where thermal stability is a priority.[53]

Despite the appeal of aramid's combination of properties, there are still barriers left to overcome that limit the widespread implementation of AFRPs. Integrating AFRPs into a wider range of environments is a challenge, due to their resistance to environmental degradation, particularly UV degradation, and their weak resistance to strong acids or alkalis.[55] Studies express that exposure to moisture or humidity can influence the mechanical performance of aramid fibres, which is a significant issue for their use in military or defence applications, such as body armour.[56] Additionally, the chemical inertness and relatively smooth surface of aramid fibres limits their ability to bind with a matrix through physical or chemical bonds, negatively

impacting the mechanical properties of AFRPs.[57] Therefore, current research is heavily focused on improving the treating the chemical inertness of aramid fibres through treatment of the surface, such as coating with nanofibres or plasma modification, to improve interfacial bonding between fibre and matrix.[57, 58] Advancements in the improvement of fibre-matrix adhesion is critical in enabling the use of AFRPs in a range of sectors, including aerospace and defence.

1.2.2 Natural Fibres

Recent literature expresses that as sustainability and environmental consciousness become a priority for industries, research is moving away from traditional composites consisting of synthetic fibres paired with polymer matrices, and is instead transitioning towards the implementation of natural fibres in composites.[7, 17] Natural fibres provide an environmentally friendly alternative to synthetic fibres, attributed to the fact that natural fibres are derived from renewable sources and more importantly, can biodegrade. Implementing generalised use of natural fibres concurrently addresses the urgency to reduce materials derived from fossil fuels and turn to a greener alternative.[59] Figure 1.8, depicting the life cycle of natural fibre reinforced polymers (NFRPs), illustrates how the implementation of NFRPs over time has the potential to improve the sustainability of material production.[60]

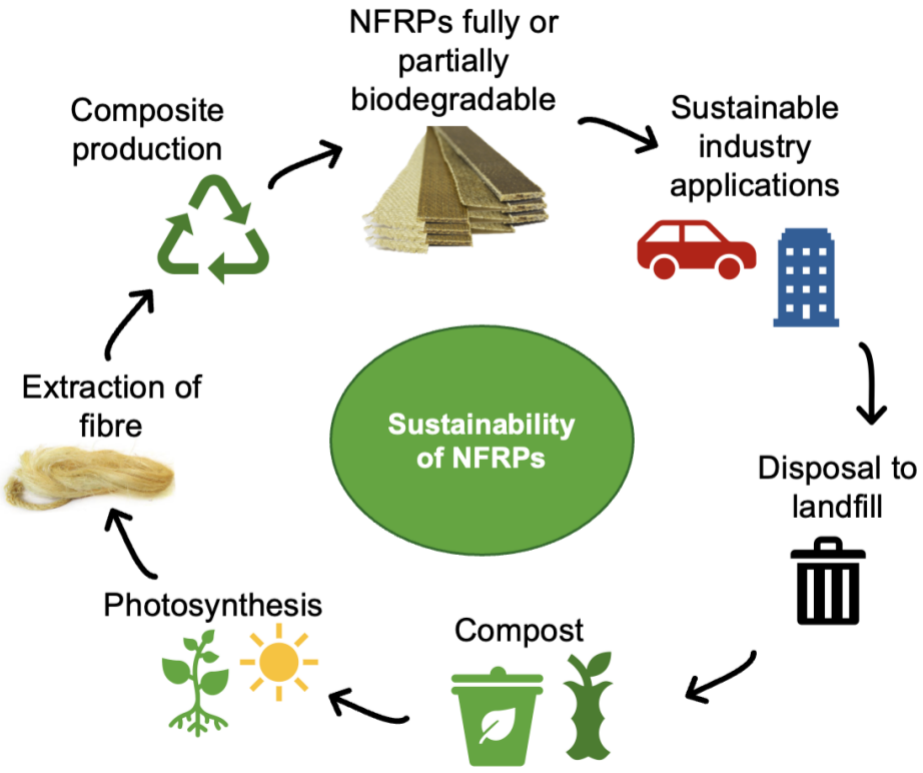

Figure 1.8: The life cycle of NFRPs, demonstrating how over time they provide a sustainable material production process. Recreated with reference to[60]

Although, in general, the tensile strength of natural fibres are lower than synthetic fibres, it is highlighted in Table 4 that natural fibres still exhibit excellent tensile strength, in addition to low density and often at a lower production cost than synthetic fibres.[15, 31, 59] Natural fibres offer lower specific weight than synthetic fibre composites, making them particularly effective when low weight is of high priority, such as in infrastructure applications.[61]

Table 4: The tensile strength of conventional synthetic fibres used in FRPs to compare with natural fibre tensile strengths. Note, the glass value is for E-glass, the carbon value is for high strength carbon, and the aramid value is regular Kevlar. The table was made with reference to[31].

Fibre material	Tensile strength / GPa	Density / (g cm^{-3})
Carbon	3.7–4.2	1.6–1.8
Glass	3.4	2.6
Aramid	2.8	1.4
Cotton	0.4	1.5–1.6
Flax	0.5–1.5	2.7–3.2
Kenaf	0.9	1.5
Sisal	0.5–0.6	1.5
Hemp	0.7	1.2

Based on their origin, natural fibres can be divided into plant fibres (which can be further divided into bast, fruit, grass, leaf, seed and stalk), animal-based fibres and mineral-based fibres, as displayed previously in Figure 1.2 [16, 59].

The current primary drawback of natural fibres is the binding of the fibres with the matrix, mainly due to the incompatibility of the hydrophilic and polar properties of natural fibres and the non-polar properties of most conventional polymers.[59] Natural fibres are prone to absorbing moisture, which not only impacts the interfacial bonding with the polymer, but also limits the applications in outdoor or moist environments.[15] Recent literature has demonstrated the interfacial bonding between the two components can be enhanced via chemical and physical treatments.

Chemical treatments consist of treatments that alter the chemical composition of the fibre. Most commonly, natural fibres can undergo an alkaline treatment using an optimal concentration of NaOH, which has been proven to improve bonding at the fibre-matrix interface and in doing so, enhance mechanical properties.[62] Additionally, an enzymatic treatment can be implemented, where enzymes, such as xylanase, are used as natural catalysts to reduce polarity of the fibres.[63] This increases compatibility of the fibre-matrix composite and minimises moisture resistance without compromising the mechanical benefits of the composites.[63] In contrast, physical

treatments target the surface topography and bonding properties of the fibre. The surface roughness is significant in addressing the compatibility of the fibre and matrix. The polymer matrix binds well to surface asperities or areas where the surface is rougher, increasing the fibre-polymer interfacial bonding.[64] Various successful methods for physical treatments have been reported, including heat treatment drying to remove moisture that affects interfacial bonding, and electrostatic discharge treatments using ionised gas, to induce electrostatic adhesion at the interface.[65]

Further barriers faced when trying to enforce adoption of natural fibres include inconsistency in results when trying to find reproducible processing methods, and inconsistent availability and quality of natural fibres in different regions.[59] However, despite these current difficulties, the extensive development into harnessing the potential of natural fibres and their various advantageous properties provides a promising future for sustainable fibre-reinforced polymers.

1.2.3 Hybrid Fibres for FRPs

Hybrid fibre-reinforced polymers involve the combination of two or more different types of fibres embedded within a single matrix, to balance the advantages and disadvantages of the fibre types.[66] For example, combining glass and carbon fibres allows for the carbon's characteristic stiffness and tensile strength to be complemented by the improved impact resistance and higher tensile strain of glass fibres, whilst simultaneously reducing costs.[67] Similarly, carbon-aramid hybrid FRPs exhibit higher tensile strength than AFRPs and a higher fracture toughness than CFRPs, conveying how hybridisation can balance desired mechanical properties within a single FRP.[68] Hybridising natural fibres with small ratios of synthetic fibres allows for the recycling possibilities of natural fibres, whilst maintaining the superior mechanical properties of synthetic fibres.[66] The combination of fibre materials in hybrid FRPs can be arranged with varying layers and orientations, as depicted in Figure 1.9.

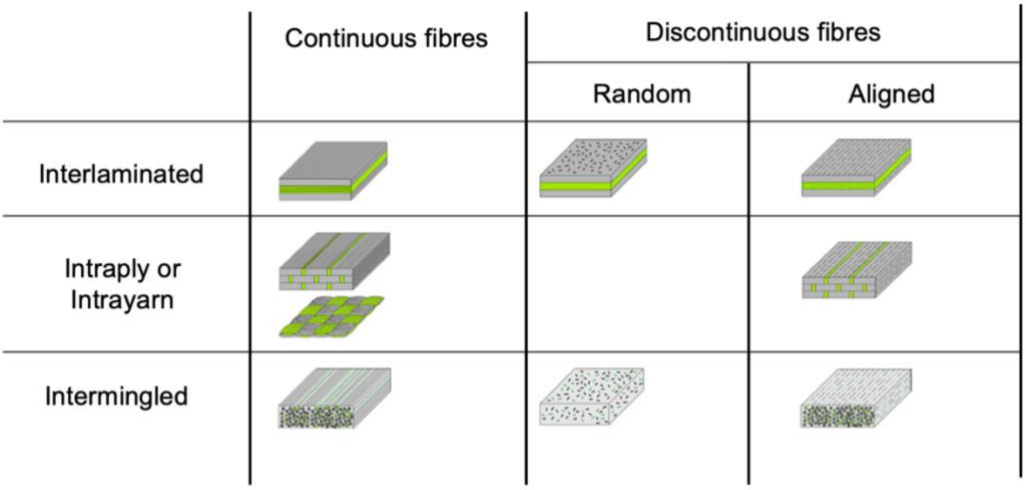

Figure 1.9: The different structures of hybrid FRPs. Adapted from[69].

1.3 Matrix materials

1.3.1 Polymer Resins

The chosen matrix will also affect the desired properties of the resulting composite. The matrix serves to protect the fibres, ensure the stress is transferred between each fibre, and essentially bind the fibres together to create the unity of the composite. Ensuring that the matrix possesses the wetting properties to ensure sufficient bonding at the fibre-matrix interface is essential, as weak adhesion can lead to fibre pull-out and interfacial debonding.[70] However, controlled debonding of the fibres from the matrix can allow improved energy dissipation and toughness, so that the composite does not shatter[70]. Frequently, a polymer is chosen as the matrix material, owing to their light weight and high strength, complemented by their low cost and availability.

Two main categories of polymer matrices exist, namely thermoplastic and thermosetting materials. Thermosetting resins are the most commonly chosen polymer matrix, due to their mechanical strength, corrosion resistance and very high thermal stability, conveyed by a high Glass Transition Temperature (T_g).[71] Figure 1.10 shows the relationship between temperature and stiffness in polymers, demonstrating how the matrix remains in a glassy state until reaching its T_g, beyond which it will transform to a rubbery state.[72] This type of resin is ideal when maintaining structural integrity at high temperatures is vital, such as in military applications.[16] Thermosetting resin undergoes an irreversible curing process, whereby permanent cross-linked polymer chains are formed, meaning the resin cannot be re-melted or re-shaped once set without causing damage to the polymer structure.[38] Although this provides the resin with high hardness, it has the downfall of brittleness upon setting[34]. Epoxy, vinyl ester and polyester are amongst some of the most popular thermosetting resins.

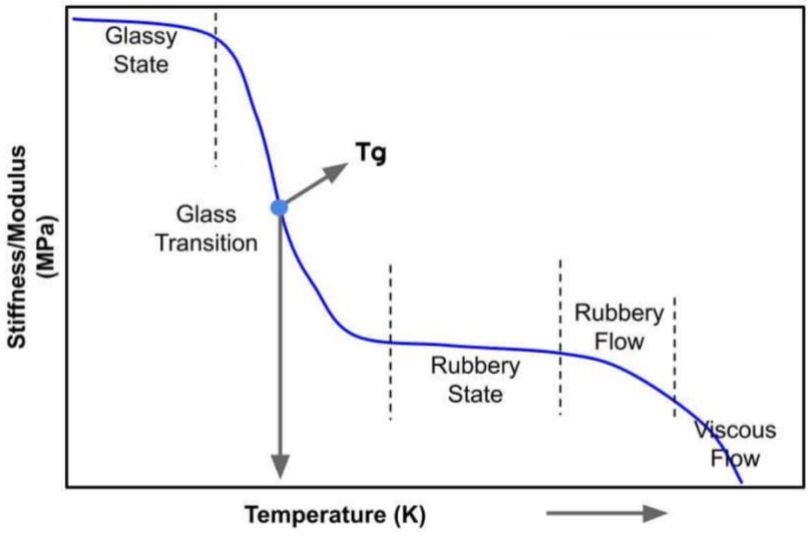

Figure 1.10: A graph depicting the relationship between stiffness and temperature for a polymer, highlighting the T_g. Image from[72].

Epoxy resins are particularly utilised in the production of high-performance FRPs due to their high thermal stability, low shrinkage upon curing and excellent chemical and moisture resistance.[17, 34, 73, 74] Additionally, epoxy resin boasts exceptional mechanical properties, including high tensile strength, stiffness, fatigue resistance and compression strength, whilst remaining lightweight.[17, 74, 75] One of the most important advantages of epoxy resins is their capability to adhere with fibres, whether natural or synthetic, enabling an exceptional strength-to-weight ratio.[17]

In contrast, thermoplastic polymers consist of linear polymer chains (Figure 1.11), interacting via van der Waals or hydrogen bonds rather than permanently cross-linked chains, which enables a reversible curing process upon heating.[71] The ability to repeatedly re-shape and re-mould the resin upon heating allows the composite to be recycled and provides flexibility within the creation of the composite. Thermoplastic polymers exhibit higher impact resistance and fracture resistance than thermosetting polymers.[76] However, binding the fibres with the thermoplastic polymer can be more challenging due its higher molecular weight and melt viscosity.[76, 77] Thermoplastic polymers, such as polyethylene (PE), polypropylene (PP) and polyethylene terephthalate (PET), offer a lower costing alternative to thermosetting polymers, but they exhibit lower stiffness and cannot withstand very high temperatures.[78] However, polyetheretherketone (PEEK) and polyether ketone (PEK) offer a high-performance thermoplastic resin with exceptional thermal stability under very high temperatures and good resistance to moisture.[34] The combination of reusability, adjustable flexibility, chemical resistance, low density and high impact resistance makes high performance thermoplastics prevalent in the aerospace industry.[78]

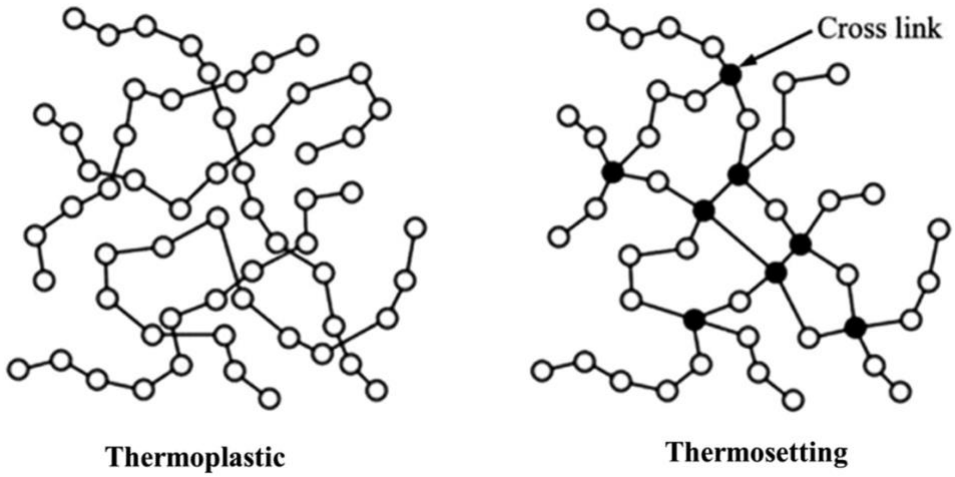

Figure 1.11: The differences in the molecular structure of thermoplastic and thermosetting polymers. Thermoplastics (left) have linear chains interacting via intermolecular forces, thermosetting (right): network of crosslinked polymer chains. Image from[79].

1.3.2 Biopolymers

Analogous to fibres, current research on matrix materials is increasingly focused on improving environmental sustainability. Polymers derived from petroleum sources not only pose environmental concerns, but involve energy-intensive extraction processes and depend on limited fossil-fuel resources.[80] Biopolymers are biodegradable polymers produced by living organisms, including plant biomass, animals, starch, lignin and plant oils.[80] Common commercially available biopolymers include polylactic acid (PLA), a synthetic biopolymer produced naturally by bacterial fermentation of starch or sugar, and polyhydroxyalkanoate (PHA), a natural polymer produced by bacterial fermentation of carbohydrate biomass.[81] Despite the benefits these alternative matrix materials present, biopolymers exhibit lower thermal stability and degradation at high temperatures, susceptibility to moisture absorption and lower tensile strength.[82] To further improve sustainability progress, biopolymer matrices are often paired with natural fibres to produce biocomposites.[80] Although there has been exploration of multiple chemical and physical treatments of the biopolymers, the limited success in the performance and environmental durability has so far been insufficient for their widespread adoption.[81]

1.3.1 Additives and Fillers

Fillers may be incorporated into the resin matrix to reduce shrinkage and prevent cracking, whilst also enhancing hardness and chemical resistance.[38] Additionally, fillers can reduce material costs through partial replacement of the resin, although higher percentage volumes of filler may induce weak interfacial bonding and particle agglomeration, leading to brittleness.[83] Additives, such as flame retardants, UV, thermal and oxidative stabilisers, nanoparticles and colour pigments are used to tailor the physical, mechanical and cost-effectiveness properties of FRPs.[9, 10, 38]

1.4 Manufacturing of FRPs

The performance of FRPs is not only dependent on the fibre or matrix material chosen, but also key variables that are considered during the manufacturing process. The alignment and lengths of fibres, fibre-volume percentage, the manufacturing processes and, as previously mentioned, the fibre-matrix interfacial bonding, all collectively influence the resulting properties of the composite.

1.4.1 Alignment and Length of Fibres

The fibre length chosen for composites can be divided into either long fibres or short fibres, namely continuous FRPs and discontinuous FRPs, respectively. Moreover, the long fibres in continuous FRPs can be aligned unidirectionally, bidirectionally (layered at angles of 0º and 90º) or multidirectional (layered at differing angles, usually in an order such as 0º, 30º, 60º, 90º, 0º),

as depicted in Figure 1.12.[84] Unidirectional alignment within a FRP provides a superior strength in the specific direction of the fibre, maximising anisotropic performance, but transverse to the fibre axis, the strength and stiffness is weak.[85] In practical applications, where multi-axial loading is of concern, bidirectional and multidirectional alignments offer a balanced performance in comparison to unidirectional composites. Multidirectional fibres exhibit a high flexibility and impact resistance option, whereas bidirectional fibres retain a high tensile strength both laterally and transversely.[84, 86] Despite generally exhibiting lower peak tensile strength, multidirectional alignment offers superior overall mechanical properties due to the ability to resist shear.[85]

In discontinuous FRPs, short fibres can be orientated randomly or aligned (Figure 1.12).[16] Discontinuous composites are generally associated with use in low performance applications, as fibre alignment is very sensitive and misalignment will severely lower the performance capacity.[87] However, development of advanced alignment techniques has demonstrated that if highly aligned discontinuous systems can be orchestrated, the mechanical properties will be comparable to that of continuous fibre composites whilst offering more accessible manufacturability.[87]

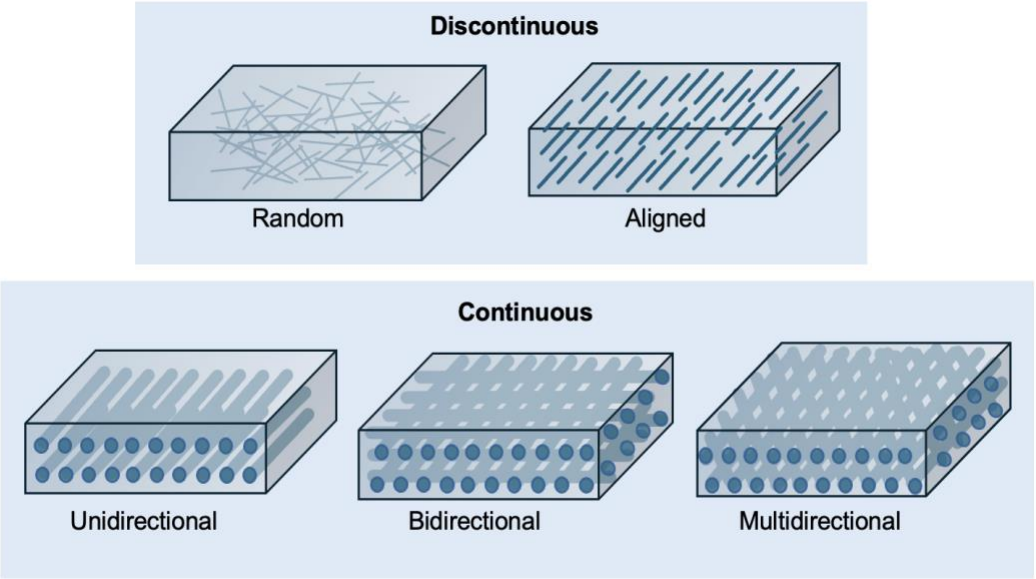

Figure 1.12: Discontinuous fibres can be organised randomly or aligned within a matrix, and continuous fibres can be aligned in a unidirectional, bidirectional or multidirectional orientation. Reproduced with reference to[4].

Continuous fibres can be in the form of unidirectional roving fibres or woven mats in a bidirectional or multidirectional orientation, providing superior load transfer and mechanical properties. In contrast, discontinuous fibres can be in the form of singular chopped fibres or a chopped strand mat, offering easier processability and flexibility. Figure 1.13 illustrates the trade-off between mechanical performance and processability with increasing fibre length and

alignment, where the highlighted region represents a compromise between these properties. The distinction between continuous and discontinuous FRPs is directly linked to the processing techniques carried out to fabricate composites.

Additionally, the fibre-matrix interfacial bonding is affected by fibre length.[31] Shorter-length fibres reduce the interfacial area available for stress transfer, making them more susceptible to fibre pull-out under stress, indicating a weaker interfacial bond.[88] Longer fibres can facilitate effective load transfer, leading to fibre fracture instead of pull-out, demonstrating that the fibre has reached its maximum tensile strength.[88] As previously discussed, chemical and physical treatments to improve the interfacial bonding between the fibres and matrix can be implemented.

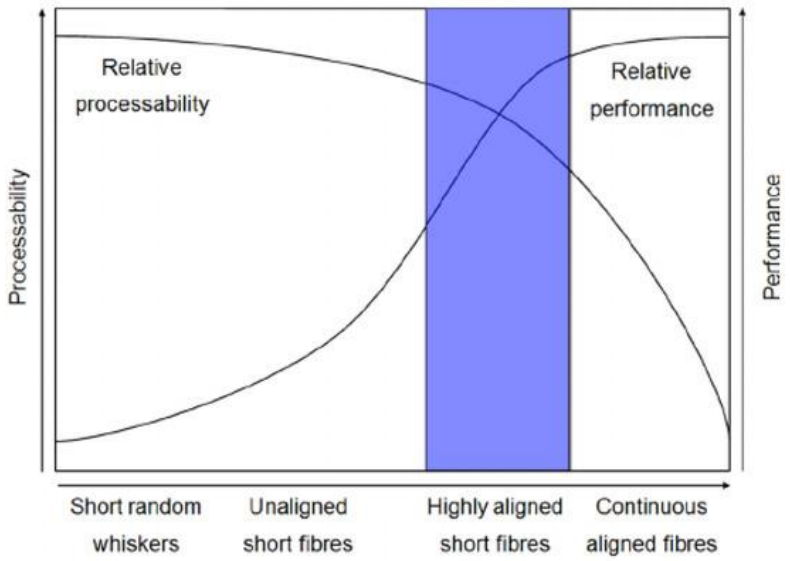

Figure 1.13: A graph to show the changes in processability and mechanical performance for fibres of different alignments and lengths. Highlighted region identifies a compromise between processability and performance. Taken from[87].

1.4.2 Fibre Loading

The fibre volume fraction in a composite is a significant parameter in determining the mechanical properties of a composite. In general, an increase in volume fraction of fibres will not only provide an increase in the load-bearing capabilities of the composite, but will also enhance the ultimate tensile strength of the composite.[86, 89] However, it is important to note that these qualities generally improve up to a specific threshold (generally above 70-80% fibre volume), beyond which mechanical performance is reduced as the fibre and matrix suffer interfacial de-bonding when the matrix cannot fully surround the fibres sufficiently.[23, 90] Impact resistance, shear strength and Young's modulus also increase with fibre volume fraction up to an optimal value.[91, 92]

The chosen fibre volume fraction for each fibre type can vary depending on the desired properties and application. Composites with a high fibre volume fraction exhibit superior strength and stiffness, therefore are utilised in high-performance composites, such as in aerospace laminates.[93] However, these composites require more demanding processing due to the difficulties associated with impregnating the fibres into the matrix. If resin flow is insufficient and cannot fully surround the fibres or infiltrate tightly packed fibres, the interfacial adhesion is reduced and defects such as voids or cracks may be introduced.[88] Composites with a lower fibre volume fraction offer high-volume processibility, lower manufacturing costs and reduced weight within a material, so are often implemented in the automotive sector.[94] The thermal conductivity of a material also improves with an increase in fibre volume fraction, particularly for highly conductive fibre types such as carbon, as a higher loading of fibres increases the available conductive pathways through the composite.[95] For general use in engineering applications, it is desirable to find a fibre volume fraction that balances the mechanical performance and processability.

1.4.3 Manufacturing processes

The production of FRPs comprises of a range of different processing techniques, each with constraints that have a direct influence on the resulting composite properties. Consequently, ensuring a balance between processability, production cost and mechanical performance is essential. In general, the process begins with the formation of a fibre preform, which is subsequently combined with a polymer matrix. These preforms are commonly produced by weaving, braiding or knitting fibres into mats or sheets.[96]

Manufacturing processes can be broadly classified into open or closed moulding techniques. During open moulding, the components are exposed to air during the curing process, whereas during closed moulding, the composite is cured under vacuum or within a closed, two-sided mould.[16] Conventional manufacturing techniques and their key characteristics are presented in Table 5.

Open moulding processes offer lower costing manufacturing techniques, but are more susceptible to formation of voids, resulting in limited control over fibre volume fraction and alignment of fibres, leading to a lower mechanical performance.[97] Hand lay-up is one of the simplest and most widely employed manufacturing processes due to its low-cost operation and ability to produce components of various geometries and thicknesses.[98] However, despite the high labour intensity required to perform the process manually, hand lay-up has a low production rate in comparison to other methods.[4] Spray lay-up offers a conceptually similar but quicker process than hand lay-up, but it provides less control over the fibre orientation and thickness.

Table 5: A summary of the principal manufacturing techniques for production of FRPs. Created with reference to[27, 96, 98, 99].

Process	Description	Type of Process	Applications	Key factors
Hand lay-up	Dry fibres are inserted into a mould by hand and resin is manually applied layer by layer using a roller or brush.	Open moulding	Storage tanks, Wind turbine blades	Simple, low-cost equipment, labour intensive, low production rate, susceptible to voids.
Spray lay-up	Similar process to hand lay-up. Chopped fibres and resin are simultaneously sprayed into a mould.	Open moulding	Large structures such as bathroom units	Simple, faster than hand lay-up, limited control of fibres, susceptible to voids.
Resin transfer moulding (RTM)	Resin injected under pressure into dry fibre preform within a closed mould.	Closed moulding	Aerospace and marine panels, wind turbine blades	High fibre volume fraction with low void content, requires specialised equipment, relatively slow curing times
Compression moulding	A charge of fibre-resin material is compressed in a two-sided heated mould using a hydraulic press.	Closed moulding	Automotive and aerospace components	Suitable balance of cost and properties for low-volume production, moderate fibre volume fraction, efficient, lower tooling cost, long run times
Filament winding	After impregnation with resin, fibres are wound around a rotating mandrel.	Closed moulding (automated)	Hollow, cylindrical parts, tanks, pipelines	Very high strength and stiffness, uniform, reduced labour
Pultrusion	Fibres are pulled through resin, followed by a heated die to shape.	Closed moulding (automated)	Structural parts, FRP bars, rods, beams	Simple and effective process, suitable for high-volume production, expensive equipment, unsuitable for shapes with varying cross-sections.

In contrast, closed moulding processes, such as RTM and compression moulding, allow for more processing control and improvements in fibre wetting, leading to composites with a higher fibre volume fraction and lower void content, directly improving mechanical performance.[27] Additionally, the RTM process can be enhanced by introducing a vacuum to pull the resin into the fibre preform. This process, Vacuum-assisted RTM (VARTM), is utilised in the manufacturing of large geometries, such as wind turbine blades or aerospace panels, and requires less complex tooling than RTM, providing a more cost-effective alternative.[16]

Automated, high-performance processes such as filament winding and pultrusion allow for high fibre volume fractions and excellent fibre alignment, resulting in superior mechanical performance.[27] Automated processes improve reproducibility and precision, although necessitate increased costs. Additionally, pre-impregnated fibres (prepreg) consist of a fibre sheet that has been pre-impregnated with partially cured resin, which can be cured upon heating.[100] Prepreg allows for precise control of a high fibre volume fraction, leading to excellent mechanical performance.[100] However, the requirement for storage at cold temperatures reduces its practicality, resulting in the utilisation of dry fabrics to offer a lower material cost and easier storage.[100] Diagrams of each of the principle manufacturing techniques mentioned can be seen in Figure 1.14.

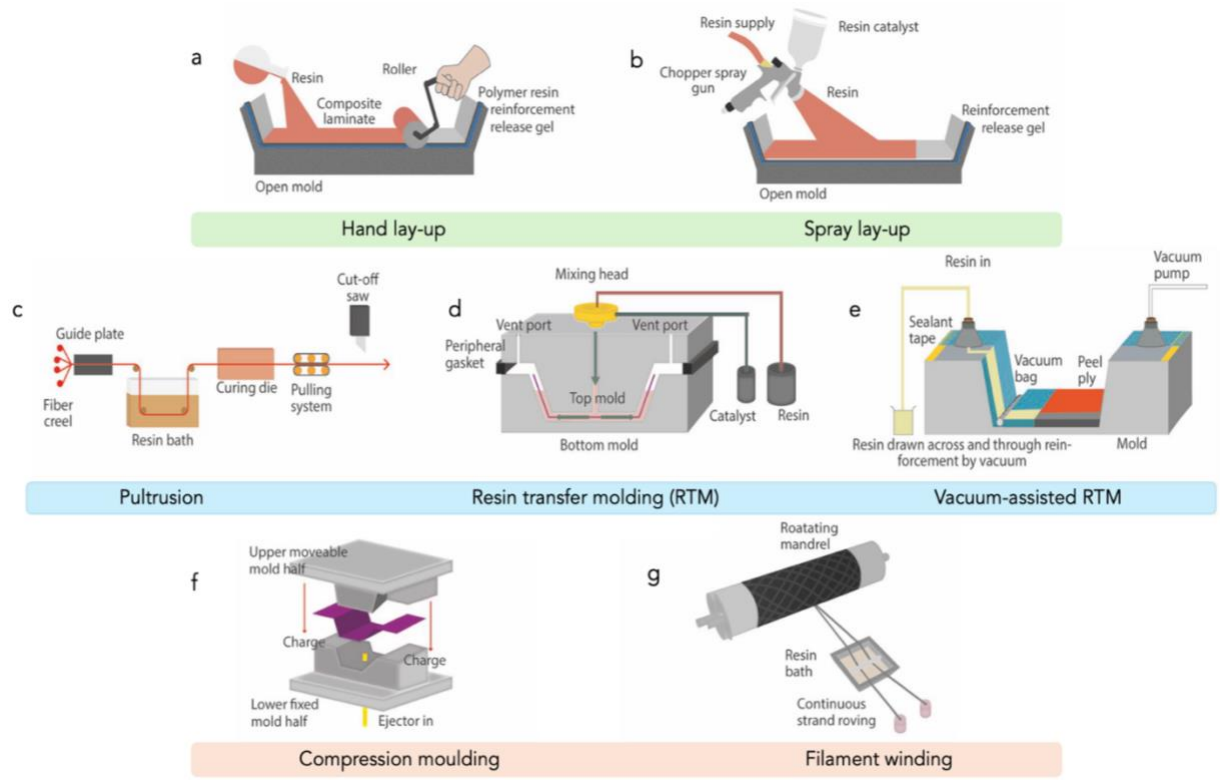

Figure 1.14: Diagrams of common conventional manufacturing techniques. a) Hand lay-up, b) Spray lay-up, c) Pultrusion, d) Resin transfer moulding (RTM), e) Vacuum-assisted RTM, f) Compression moulding, g) Filament winding. Image edited and rearranged from[4].

1.5 Diamond

Although long upheld for its aesthetic and materialistic purposes, diamond possesses an exceptional combination of chemical, physical and mechanical properties, making it an ideal candidate for advanced reinforcement purposes. Diamond is recognised as the hardest known naturally occurring material and boasts an extremely high Young's Modulus, additionally making it one of the stiffest natural materials.[101] Furthermore, diamond exhibits the highest thermal conductivity at room temperature, a very low thermal expansion coefficient, excellent wear resistance and strong chemical inertness to most reagents.[101] The origin of many of these properties lies in its sp^3 hybridised lattice structure of carbon atoms, as illustrated in Figure 1..

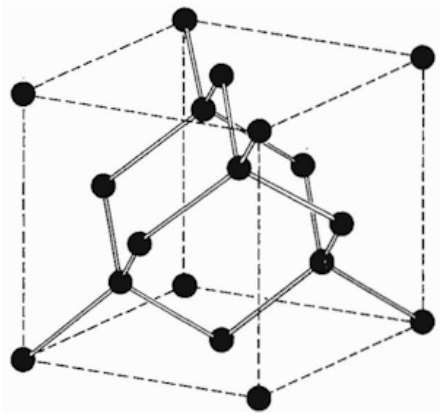

Figure 1.15: The structure of a diamond lattice, demonstrating each carbon atom tetrahedrally orientated. Diagram taken from[102].

Collectively, its remarkable properties clearly distinguish diamond from conventional reinforcement materials. However, the scarcity of natural diamond and difficulties surrounding its extraction have historically limited its use in widespread applications. The ability to produce synthetic diamond presents a solution to this limitation**.**

1.5.1 Synthesis of Diamond

For over 200 years the knowledge that diamond is formed solely of carbon atoms has been widely recognised; however, its synthesis proved difficult due to the extreme conditions necessary for its formation.[103] Early synthetic diamond formation was achieved through a High Temperature High Pressure (HTHP) process, first demonstrated in 1955 by General Electric.[104] HTHP replicates the conditions of natural diamond formation, by converting graphite to diamond

under high temperatures and pressures. However, the specialised equipment required and the restricted size of the growths, limit its broader application.

1.5.1.1 Chemical Vapour Deposition (CVD)

Early forms of low-pressure diamond synthesis were pioneered by Eversole in 1958 and Deryagin *et al.* in 1968, followed by the commercial emergence of Chemical Vapour Deposition (CVD) techniques in the 1980s.[105, 106] CVD methods, including Hot Filament CVD (HFCVD) and Microwave Plasma CVD (MWCVD), provided an efficient and cheaper alternative to HPHT, offering greater control over morphology of the surface.

During CVD, diamond is deposited onto a surface through chemical reactions of gaseous precursors at high temperatures in the range 700-1000 ºC.[107] A carbon containing gas, methane (CH_4), and hydrogen (H_2) are introduced into a chamber held under low-pressure conditions. The hydrocarbon mixture of gases undergo activation via an energy source, a heated filament in the case of HFCVD, or a microwave-generated plasma for MWCVD, producing reactive carbon species which diffuse towards the surface of the substrate. Atomic hydrogen selectively etches away non-diamond carbon allotropes, such as sp^2 bonded graphite, and promotes the formation of sp^3 bonded diamond.[107]

MWCVD typically produces higher quality diamond films and offers negligible contamination risks, but involves very high operating costs, and is therefore generally reserved for applications when high purity diamond film is essential. In contrast, HFCVD offers lower operating costs and greater freedom over film geometry and morphology, making it ideal for diamond growth on wires.

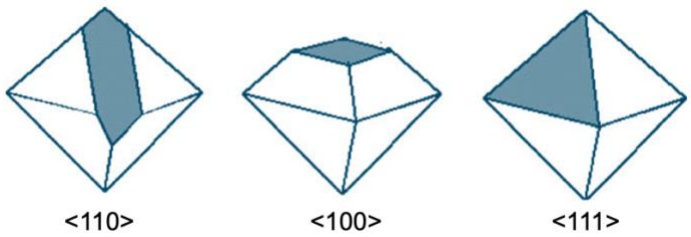

Figure 1.16: Diagrams of common diamond crystal orientations present in CVD diamond films, adapted from[108].

The specific growth conditions implemented during CVD ratio are directly linked to the resulting morphology of the diamond film. In particular the CH_4:H_2 ratio and temperature influence the resulting diamond film, allowing control over whether it is randomly orientated or exhibits specifically dominating crystal orientations, such as <111> and <100> facets, seen in Figure

1.16.[109] For example, a study varying the CH_4 concentrations for the growth of diamond coated wires demonstrated a transition from <111> to <110> orientation with an increase in CH_4 concentration: at a 0.5 % CH_4 concentration, the <111> orientation dominated, transitioning to a mixed structure of <110> and <111> at 0.75% CH_4 and finally, a predominately <110> orientation at 1% CH_4.[110]

1.5.1.2 Substrate choice and Preparation

During heteroepitaxial growth, where the substrate is non-diamond, the extent of adherent diamond growth depends on the substrate's ability to form a carbide layer prior to the diamond nucleation.[111] A carbide layer is a thin coating that forms on the substrate prior to diamond growth, consisting of a compound of carbon and typically a metallic element. The carbide layer thickness deposited on differing materials may vary and impact resulting properties of the substrate, especially in the case of thick layers. For example, in titanium (Ti) substrates, the continued growth of TiC during deposition can cause the diamond film to swell and crack, limiting diamond film thickness.[112] Most substrates suitable for carbide formation are metals like tungsten, tantalum, aluminium and other rare-earth metals, but non-metal substrates such as boron or silicon or carbide-containing substrates can be used.[101]

Non-carbide forming metals such as Copper (Cu) can be used as substrates for diamond growth, however, the resulting diamond film is not adherent and can be removed from the substrate with ease to use independently.[112] In contrast, certain metals have such a substantial reaction with carbon that they are effectively comparable to a carbon sink, inhibiting diamond formation.[101]

Furthermore, the substrate chosen for CVD growth must have a melting point exceeding the temperature at which diamond growth takes place, and a thermal expansion coefficient similar to diamond, to account for the expansion of the diamond and substrate during the growth.[101] Tungsten is a particularly appropriate choice for the CVD growth of adherent diamond, as it forms a sufficient carbide layer, without reacting too readily to carbon, ensuring that the diamond layer can form.[112] Additionally, tungsten has a very high melting point, a low coefficient of thermal expansion and is commercially available in varying diameters.

Pre-seeding a non-diamond substrate with diamond particles, for example via manual abrasion, significantly facilitates diamond growth by increasing the density of nucleation sites, reducing the nucleation time and promoting faster continuous film formation.[107] This process is usually carried out via manual abrasion or ultrasonic agitation.

1.6 Diamond-coated fibres as an advanced reinforcement material

While early developments in CVD focused on planar film deposition, the CVD process enables uniform deposition onto a range of substrates, including metal or ceramic wires, with tungsten commonly used due to its favourable properties. Since the successful expansion into the coating of thin wires in 1991,[113] it has be demonstrated that a stiff fibre with a high Young's modulus can be formed, with diamond coatings of the order of 100 μm reported.[114]

CVD diamond coatings have since been successfully deposited on various fibre materials, including silicon carbide (SiC), copper (Cu) wires with diameters under 100 μm and tungsten (W), typically using standard conditions of 20-40 Torr and 0.5-1.25% CH_4 in H_2.[115] Cu substrates allow the fabrication of free-standing, hollow diamond tubes (Figure 1.17) by selectively etching away the Cu core with an appropriate acid.[112] Additionally, despite the issues associated with their high etching rate and low nucleation density,[116] carbon fibres have also been successfully coated with CVD diamond.[117] Nevertheless, recent investigations show that atomic hydrogen etching of the carbon fibre still remains a significant challenge.[118]

It has been widely reported that the thermal conductivity of CVD diamond films can reach values close to single crystal diamond, provided the growth is of high quality and contains large grains.[119, 120] The fundamental heat transport system within diamond's crystal lattice is dominated by lattice vibrations, phonons, leading to this extremely high thermal conductivity. However, scattering at grain boundaries can disrupt this primary mechanism, outlining the need for a consideration towards grain size and grain density.[121]

This development provides a clear pathway to directly exploit the mechanical properties of diamond through the fabrication of diamond fibres for incorporation into a matrix material to create a fibre-reinforced composite. Table 6 illustrates the remarkable properties of CVD diamond-coated wires in comparison with conventional fibres.

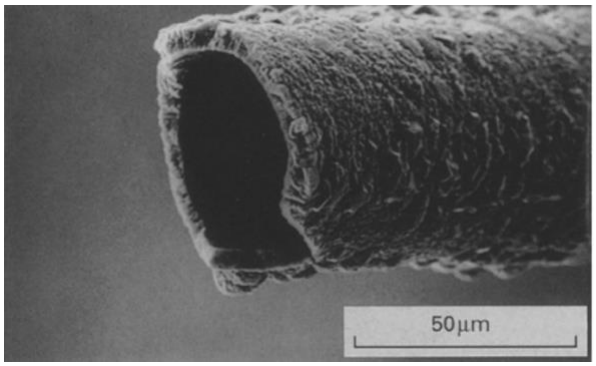

Figure 1.17: A hollow diamond fibre of 5 μm thickness after growth on Cu wire and etching away with nitric acid. Produced by P. W. May *et al.* in 1994. Image from[114]

Table 6: The exceptional properties of natural diamond in comparison with CVD diamond, diamond-coated W fibres and other conventional fibres. Note, thermal conductivity range of CVD consist of mean values with variations due to anisotropy in CVD diamond films. Literature values reported using[120, 122, 123], unless specified otherwise.

Material	Young's Modulus / GPa	Tensile Strength / GPa	Thermal Conductivity / (W m^{-1} K^{-1})	Density / (g cm^{-3})
Natural diamond	1050	~ 3.5	600 – 2500	3.51
Synthetic CVD diamond	700-1000	0.5 – 1.4	1000 – 2200	3.5
Diamond fibres (50 µm diamond, 100 µm W wire)	~ 800	1 – 2	750-900[121]	7.4
Carbon fibre	230	3.5	105	1.76
(E-Glass) Glass fibre	73	3.4	1	2.60
Tungsten fibre (150 µm)	410	2.7	170	19.3

1.6.1 Diamond-Metal Matrices

Diamond fibres embedded into metallic matrices, namely Diamond Metal Matrix Composites (MMCs), have previously been explored due to their high stiffness and low weight, with titanium or aluminium used as the matrix material.[124] For example, CVD diamond-coated W spiral wires have been incorporated into aluminium matrices to enhance thermal conductivity for thermal management applications.[119] However, it has been widely reported that fibres embedded into metal matrices required surface treatment in the form of 'sputter coating' to ensure uniform distribution within the composite and sufficient interfacial bonding, inducing an increase in the processing time and cost.[124] Additionally, for any impactful increase in stiffness, a high volume fraction of diamond fibres had to be added to the metal matrix, further increasing expenses. In recent work, diamond particles have been used to reinforce metal matrices, but these similarly require high volume fractions (above 70%) to achieve significant enhancements in properties, in particular, thermal conductivity.[119] In contrast, replacing the metal matrix with polymer offers a more efficient alternative to harness the properties of diamond.

1.6.2 Diamond-Polymer Matrices

Diamond FRPs provide an extremely stiff and strong alternative to MMCs, with an even lower density. Significant improvements in stiffness and thermal conductivity can be obtained at a

comparatively low fibre volume fraction, with only a small number of fibres required for noticeable difference.

Research into diamond FRPs is relatively limited, with early developments rooted in the University of Bristol's diamond laboratory. It was there in 2001, that the first diamond fibre-reinforced polymer was produced, consisting of a 100x20x5 mm poly(methylmethacrylate) block reinforced with continuous, unidirectional fibres (Figure 1.18).[122] At a fibre volume fraction of 1%, the composite reportedly displayed an increase in Young's modulus by a factor of 6.[122]

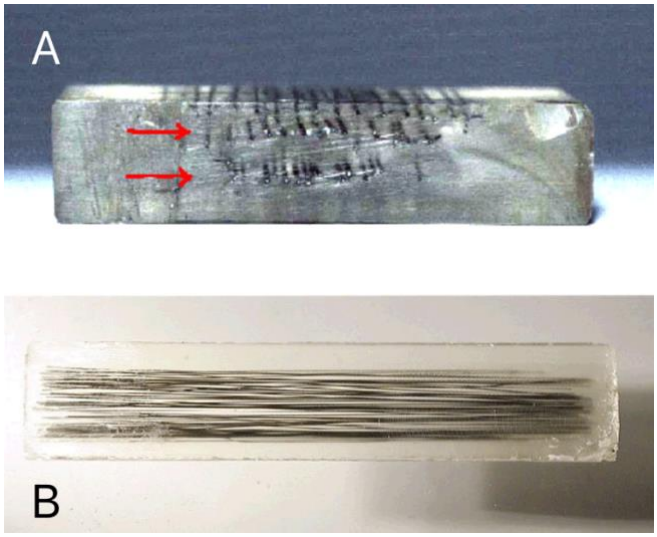

Figure 1.18: The first diamond fibre reinforced polymer, produced at the University of Bristol Diamond Laboratory in 2001. Image taken from[122].

These high-performance diamond FRP exhibit exceptional strength-to-weight ratios and high stiffness, making them ideal for advanced engineering applications, such as aerospace components where low weight but excellent mechanical performance is critical. Additionally, the high thermal conductivity of diamond provides potential for thermal management applications, such as 'heat pipes', where heat is efficiently conducted along the fibre direction to a heat sink, whilst remaining electrically and thermally insulating to its surroundings.[121] The comparatively low thermal conductivity polymer acts to reduce outward heat loss, which would be advantageous in electronic devices where other components could get damaged by heat dissipation.

However, several challenges currently limit the widespread implementation of diamond fibres for use in FRPs. Diamond is chemically inert, leading to potentially poor interfacial adhesion with polymer matrices and consequently lowered mechanical performance. Additionally, diamond fibres are characteristically brittle, presenting the increased risk of fracture under stress and limiting the ability to be woven or bent.[125]

The implementation of these fibres into a polymer matrix to produce diamond FRPs is further constrained by processing challenges. For applications where the composite requires high thermal stability, high T_g polymers, such as thermosetting polymers, are required, but these typically exhibit high processing viscosities and call for high manufacturing temperatures.[34] Furthermore, with an average growth time of 0.5 μm h^{-1} in a hot filament (HF) reactor, the CVD process is relatively slow, limiting the potential for scaling up to high-volume production. The need for specialised equipment, induces high manufacturing costs, providing a potential barrier for the general adoption of diamond fibres due to the limitations on the projects they can be used in.

1.7 Aim and objectives of this thesis

The initial objective of this thesis was to convert the Thomas Swan reactor, a large HF reactor, from its current version for large, planar substrate areas, to its former use, specifically for deposition onto wires. Following this, the overall aim of the project is to establish a reliable process for producing diamond-coated wires, by coating tungsten wires of 100 μm in HFCVD polycrystalline diamond.

Alongside the Thomas Swan modifications, six 10 x 10 mm silicon (Si) wafers will be coated in polycrystalline diamond via HFCVD for initial adhesion testing of diamond with selected polymers. These diamond-coated Si wafers will provide a planar surface area to perform adhesion testing, as the geometry and curvature of the diamond-coated wires prevents the reliable use of the adhesion testing equipment.

Additionally, tungsten wires of 100 μm will undergo HFCVD diamond growth in the HF reactor, for comparison with diamond-coated wires produced in the Thomas Swan reactor. This allows a control to give an indication of the quality of diamond produced, particularly as the Thomas Swan reactor has not been in use for an extended period of time.

2. Experimental

2.1 Modification of the Thomas Swan Reactor

The Thomas Swan reactor was assessed to identify the modifications that needed to be made for the conversion to depositing diamond onto wires, instead of larger substrates. In its previous form, the wafer substrate is positioned in front of multiple tungsten filaments, allowing for deposition on larger substrates. In its wire-coating mode, the chamber holds two tungsten filaments, both surrounded by a wire carousel that can simultaneously coat 20 substrate wires, as illustrated in Figure 2.1. The filament wire and the substrate wires are held under tension to avoid bending or movement and ensure uniform growth.

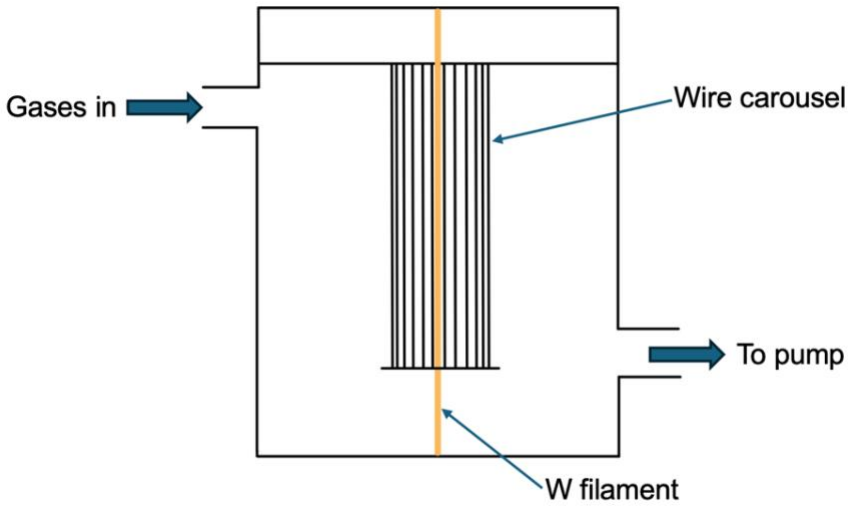

Figure 2.1: A schematic of the Thomas Swan reactor in wire mode. The wire carousel holds 20 wires of thickness 50-100 μm, each 5 mm apart and held under tension by spring-loaded clamps.

As the primary differences between the two modes are the components extending from the lid, the first step was switching to the appropriate chamber lid for the wire mode. Additionally, a custom-made C-shaped bracket was fitted onto the lid of the reactor chamber and attached to the pneumatic for more stability when lifting the lid. Figure 2.2 shows an image of the reactor lid before (left) and after (right) the C-shaped bracket was added.

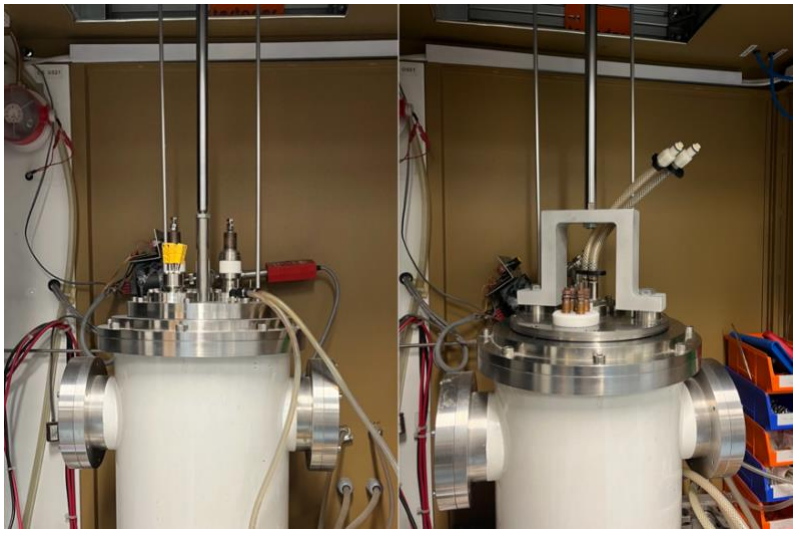

Figure 2.2: On the left, the previous lid for the large substrate form of the reactor. On the right the lid for wire-mode with the new, C-shaped bracket fitted for attachment to the pneumatic.

The performance of the vacuum pump was tested to ensure the chamber could be reduced to an appropriate vacuum when pumping down. A stable reading of 5 x 10^{-2} torr was acquired on the pressure gauge, which is appropriate for initial operation to ensure the composition of gases in the chamber is well-defined during growth through the removal of residual gases.

Figure 2.3: Full image of the Thomas Swan Reactor: the large chamber on the right and the operating panel on the left.

General maintenance and evaluation of the reactor and its components was carried out: the springs on the wire holders were replaced, the dual filament control panel was repaired as the trip reset button was not responsive, and a new Pirani 501 gauge was installed to accurately measure the low vacuum pressures in the chamber. The barometer was verified against atmospheric pressure, as any error in this reference may lead to error in the chamber pressure readings. Additionally, the electronics of the mass flow controller, used to measure and control the mass flow rate of gasses entering the chamber, were inspected for any faults. Figure 2.3 shows a full view of the Thomas Swan, including its operating panel and chamber for CVD growth.

2.1.1 Water-cooling system

In the large-area substrate configuration of the Thomas Swan reactor, the external chiller unit required was much larger than necessary for operation in wire deposition mode, therefore the chiller was replaced with a lower capacity system. Consequently, this provided an opportunity to re-organise the water-cooling network as illustrated in Figure 2.4. A custom-made manifold was fitted at points where the tubing from the chiller split into two and the internal diameter was reduced, facilitating the cooling of the lid and the chamber body separately but simultaneously.

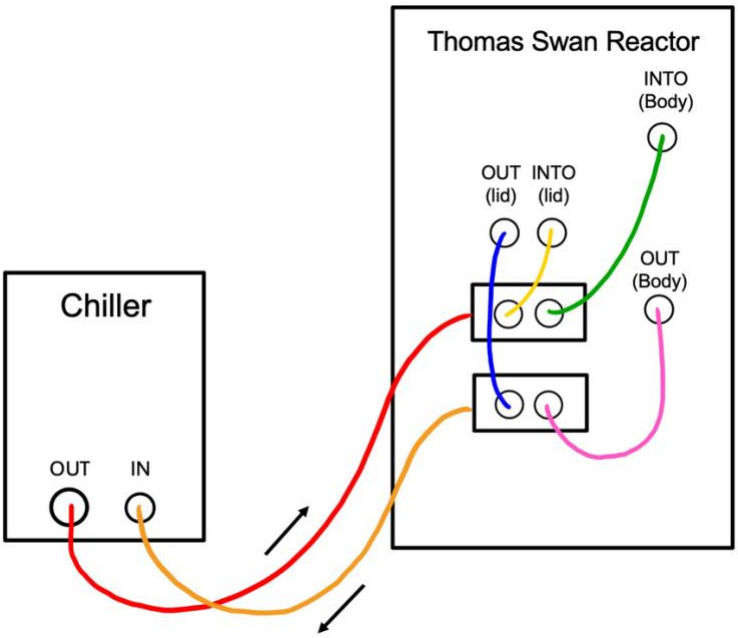

Figure 2.4: Diagram of the Thomas Swan reactor water-cooling system. The water flows out of the chiller (red) to the manifold where it is split into the lid (yellow) and body (green). After, the water flows out of the lid (blue) and the body (pink) and back into the chiller (orange).

Throttle valves were integrated into the plumbing system to enable control of the water flow to both the lid and body if required during a CVD growth. These valves were purposely chosen to

have detachable screw-on handles so the handles could be removed if deemed necessary, to avoid any accidental changes to the set flow conditions. The threads of each pipe connection were standardised to G ½ (British Standard Pipe Parallel) fittings and, where appropriate, sealed with polytetrafluoroethylene (PTFE) tape to provide watertight protection. The originally transparent tubing was replaced with yellow, opaque tubing to prevent the accumulation of algae caused by light transmission through the tube. Additionally, the tubing was purged with detergent and deionised water to ensure a consistent and clean flow of water throughout the cooling system.

The predicted growth rate of the Thomas Swan is 0.5-1 μm h^{-1} but due to the interlock system, as seen in Figure 2.5, the reactor has the capability to be left continuously running for multiple days. Therefore, to conclude the modifications made on the Thomas Swan reactor, the interlock system was tested with only the filaments present, by simulating a series of circumstances designed to trigger the machine to act accordingly:

- The water flow was purposely reduced, triggering the immediate ceasing of the heat to the filaments and the chamber heater. Note, argon does not flow into the chamber because the loss of water cooling is a thermal management issue, rather than an issue with the contents of the chamber. Also, the inconvenience it would cause if it were to happen every time the water was turned off when pumping down to vacuum, would be unnecessary.
- In the case of the lower cabinet door opening, the filament power and the chamber heater cease and argon floods the chamber.
- The additional interlock options, reactor chamber, extract air and pressure would also cause the power to the filaments and the chamber heater to turn off and argon to purge the chamber if necessary.

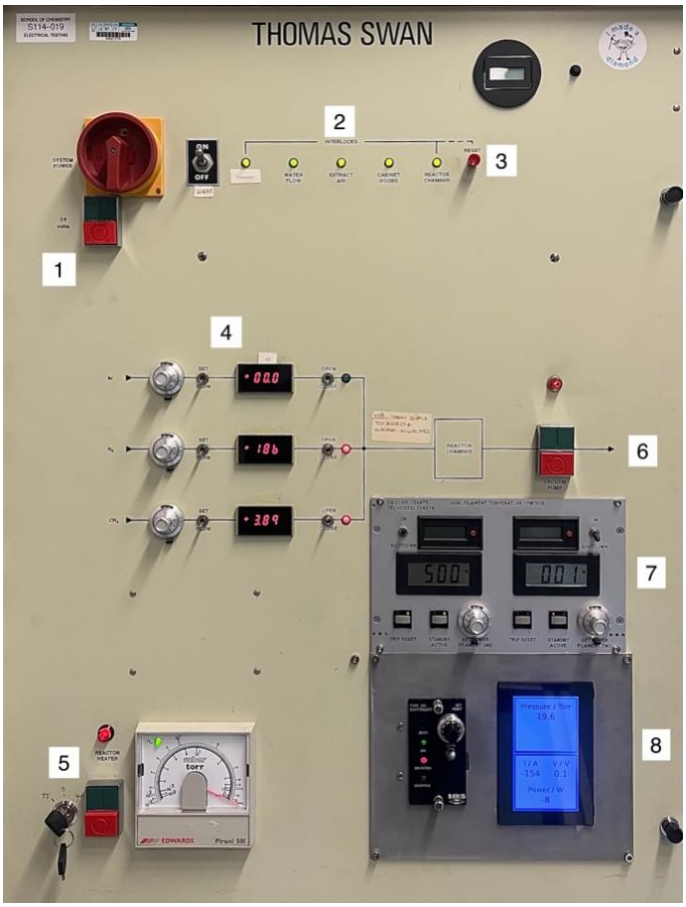

Figure 2.5: A close up of the Thomas Swan operating panel to the left of the machine. 1) power switch for entire system, 2) interlock system, including indicator lights, 3) interlock reset switch, 4) controls for gas flow, 5) reactor heater switch, 6) switch for vacuum pump, 7) control panel for filaments, including heating switch and power dials, 8) chamber pressure control panel.

2.2 Preparation and Growth of Diamond Fibres

2.2.1 Fabrication of 10 x 10 mm Diamond-Coated Silicon Wafers

Six 10 x 10 mm silicon (Si) wafers of thickness 525 µm were coated in polycrystalline CVD diamond to provide a planar surface for adhesion testing, as the small diameter and curved surface of diamond fibres would prevent the use of the pull-off tester equipment. The Si wafers were cut using the Oxford Lasers Alpha 532-XYZ-AU micromachining system and cleaned via ultrasonication in acetone for 5 minutes, followed by 5 minutes of isopropanol (IPA). The samples were pre-seeded by the manual polishing of the substrate surface using Vanmoppes diadust, diamond powder (particle size 1-3 µm) with a piece of Si as the abrasive medium. This process facilitated the embedding of diamond particles into the surface, increasing the density of nucleation sites (Figure 2.6). Following this, the pre-seeded Si substrates were cleaned again using IPA and airdried with an air gun.

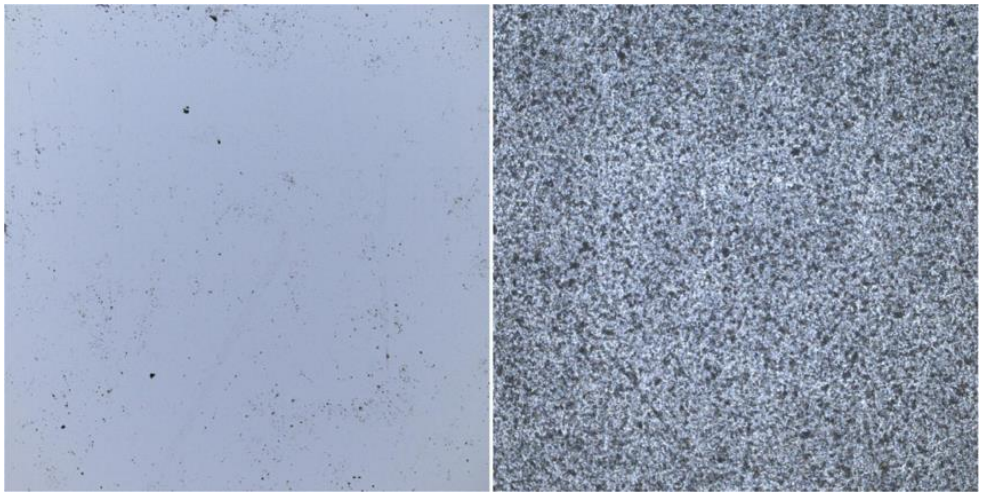

Figure 2.6: On the left, the Si wafer before the seeding process of manual abrasion of diamond powder. On the right, the Si wafer after the seeding, where the darker areas can be identified as the embedded diamond particles. Images taken using the Olympus LEXT OLS5100 Laser Microscope.

The growth on the six pre-seeded Si samples was carried out in runs of two Si wafers at a time, using the HF reactor, seen in Figure 2.7, with a predicted growth rate of around 1 μm h^{-1}. The conditions implemented during the growth are as illustrated in Table 7, with each substrate at a distance of 3 mm from the filament. The filament material was tantalum, used to withstand the very high temperatures required. A CH_4 concentration of 1% relative to H_2 was maintained as higher CH_4 concentrations (~5%) are reported to typically decreases grain size to the nanometre scale, resulting in a high grain boundary density and a much smoother surface, compromising adhesion[126]. A schematic of the hot filament reactor is illustrated in Figure 2.8.

Table 7: The conditions required for a 6-hour growth on 10 x 10 mm pre-seeded Si wafer substrates.

Pressure / Torr	Substrate Current / A	Filament Current / A	H_2 Flow / sccm	CH_4 Flow / sccm	Filament Temperature / ºC	Time / h
20	4	25	200	400	2000	6

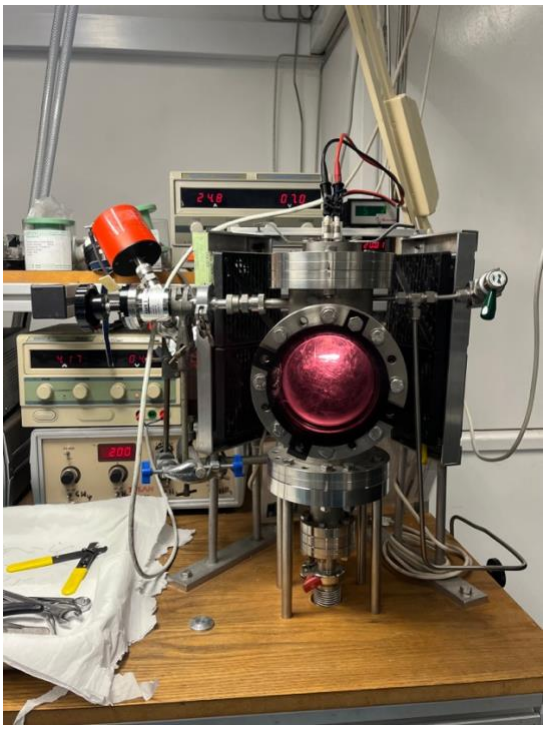

Figure 2.7: Hot filament reactor used for CVD growth on planar Si wafers.

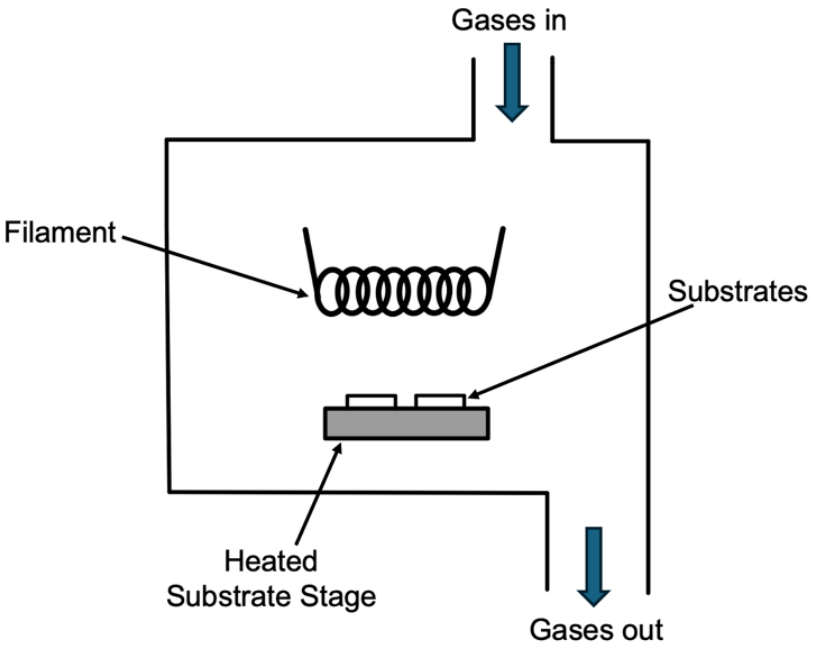

Figure 2.8: A schematic of the hot filament reactor, including the Si wafer substrates.

2.2.2 Initial Adhesion Testing of Diamond-Coated Si Wafers

The diamond-coated 10 x 10 mm Si samples provided a surface to test the adhesion properties of diamond with available polymers, to give insights and direction for future incorporation of diamond fibres into a polymer matrix in FRPs. Initially, finding an appropriate high Tg polymer was prioritised, as the intention was to use the resulting FRP in thermal management applications. However, due to time constraints during the laboratory time allocated for this project and logistical difficulties encountered with the resin bonding process at the National Composite Centre (NCC), the most viable options were commercially available Bisphenol A epoxy compounds (BPAs), namely Bisphenol A epichlorhydrin resin (Resin A, for simplicity) and Bis-[4-(2,3-epoxipropoxi)phenyl]propane resin (Resin B).

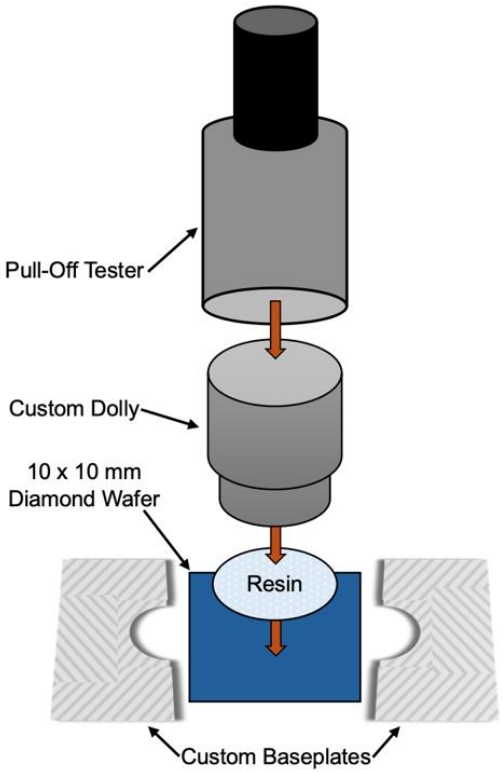

Figure 2.9: The set-up designed to measure the adhesion between the chosen resins and the diamond-coated Si wafer. Firstly, the resin was applied, followed by the dolly. Once set, the pull-off tester is applied to give the adhesion results.

The set-up to measure the adhesion properties is illustrated in Figure 2.9. Four of the diamond-coated Si samples were coated in a thin layer of epoxy: two samples with Resin A and two samples with Resin B. Following this, the aluminium dolly was adhered to the resin, as in Figure 2.10. A standard aluminium dolly of diameter 10 mm was reduced to a custom size diameter of 8 mm for compatibility with the wafer. For ease when using the pull-off tester, custom baseplates with an inner diameter of 8.7 mm, was created to provide a surface and clamp the sample down. Pull-off testing was carried out using a PosiTest AT-A Automatic Pull-Off Adhesion Tester,

which employs an electronically controlled hydraulic pump to apply a continuously increasing pull-off pressure. Once the resin had set and the dolly was securely adhered to the diamond surface, the baseplates were inserted around the dolly, before the tester was inserted over it, to provide a quantitative reading of the force needed to remove the polymer from the diamond surface.

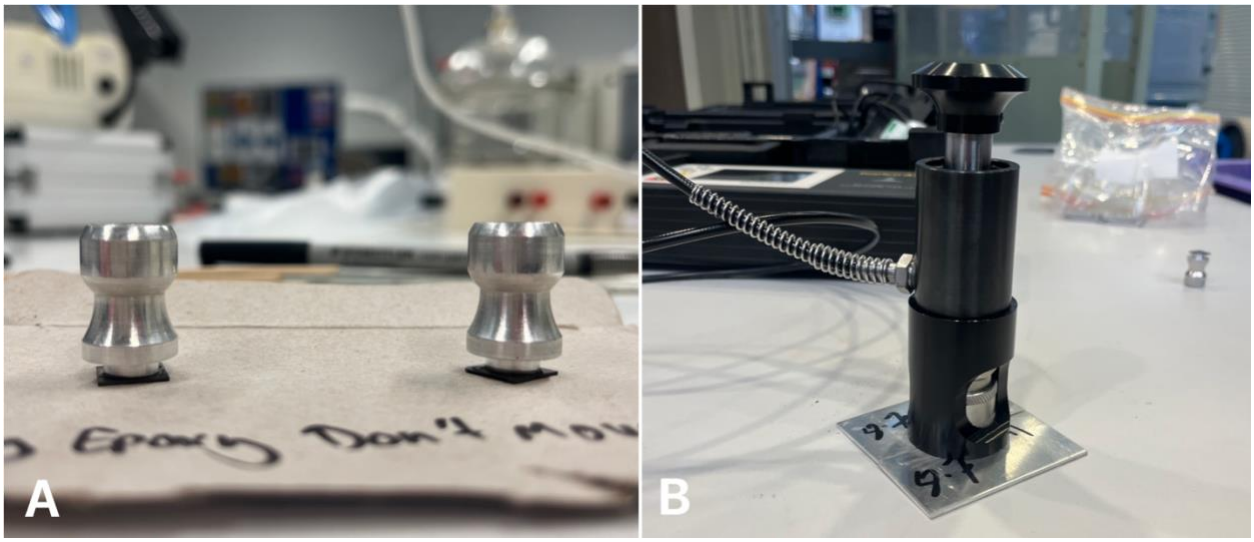

Figure 2.10: A) The aluminium dollies adhered to the diamond coated Si wafer: one sample with Resin A and the other with Resin B. B) An image of the PosiTest AT-A Automatic Pull-Off Adhesion Tester, with the aluminium dolly enclosed and the baseplates on top of the sample.

2.2.3 Fabrication of Diamond-Coated Tungsten Wires using the Hot Filament Reactor

Whilst the Thomas Swan machine was undergoing modifications, the Hot Filament reactor (Figure 2.7 and 2.8) was used to deposit undoped diamond onto tungsten wires. This was primarily for two purposes: firstly, to ensure we had diamond-coated fibres for analysis, in preparation of circumstances out of our control that may prevent operation of the Thomas Swan during the project timeframe and secondly, to provide a baseline for comparison with the wires coated using the Thomas Swan machine if the modifications were successfully completed in time.

No manual pre-seeding was required for the tungsten (W) wires, unlike the Si substrates, as during factory production, the W wires are drawn through a diamond die, essentially pre-seeding the surface of the wire systematically. Three W wires were included in the deposition, arranged as in Figure 2.11 with each wire under one of the three filaments. The conditions employed to coat the tungsten wires can be seen in Table 8, with each wire at a distance of 3 mm from the tantalum filament.

Table 8: The conditions required for an 8-hour CVD growth on 3 tungsten wires in a hot filament reactor.

Pressure / Torr	Substrate Current / A	Filament Current / A	H_2 Flow / sccm	CH_4 Flow / sccm	Filament Temperature / ºC	Time / h
20	4	25	200	400	2000	8

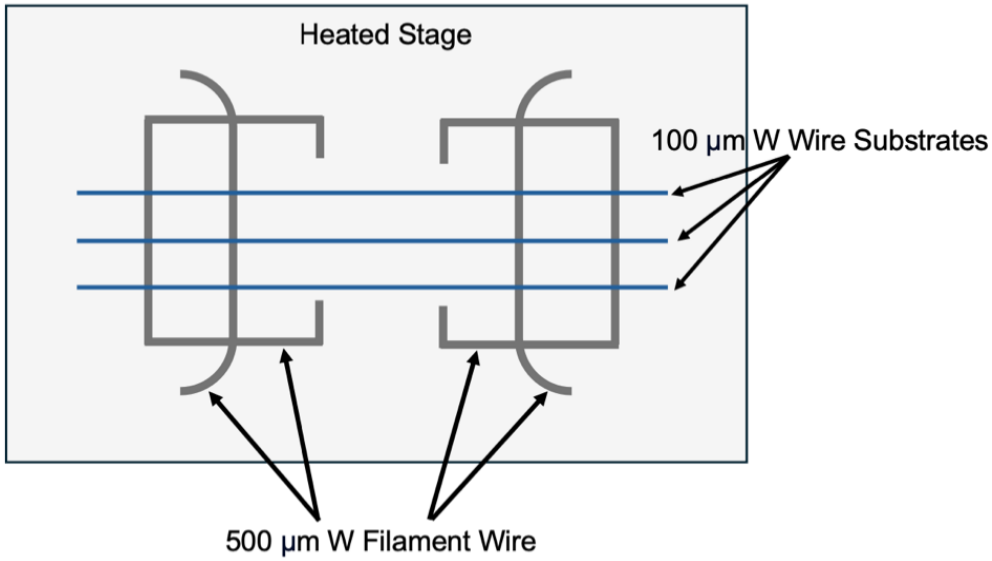

Figure 2.11: The arrangement of the W wires in the HF reactor for CVD deposition. Each of the W wire substrates was positioned under one of the three filaments in the reactor.

2.2.4 Fabrication of Diamond-Coated Tungsten Wires using the Thomas Swan Reactor

Following the conversion of the Thomas Swan reactor into a mode suitable for CVD growth on wire substrates, two trial runs were able to be performed in the time available. The wire carousels were loaded with tungsten wires of 100 µm diameter by threading them through the holes of at the top and securing them under tension by spring-loaded screw clamps. The bottom clamps then screw straight into the clamp. The wire carousel is attached so the filament runs parallel to the wires, located centrally from each one, as demonstrated in Figure 2.12 (and previously in Figure 2.1), where the chamber lid has been lifted to facilitate this.

Figure 2.12: With the chamber lid lifted via the pneumatic, the wire carousel can be attached onto the filament, before the lid is lowered back into the chamber.

The conditions outlined in Table 9 were implemented for both trial growths. Although the Thomas Swan reactor is designed to be left running for around 72 hours, the risks associated with an unattended run this early on were not possible to overcome in the timeframe. Therefore, the first growth was 8 hours, so that the reactor could be monitored throughout. Due to constraints regarding leaving the reactor overnight, the second growth was carried out in three cycles of around 6-7 hours before being shut down (filaments turned off, pumped back down to vacuum) until the next day where the growth was restarted with the same conditions. By implementing this method, the growth time totalled 20 hours.

Table 9: The standard conditions used for the first two trial runs of the Thomas Swan after its modifications, with one wire carousel present, filled with 20 W wires.

Pressure / Torr	Power per Filament / W	H_2 Flow / sccm	CH_4 Flow / sccm	Chiller pressure / bar
20	500	200	400	4

2.3 Characterisation Techniques

2.3.1 Laser Raman Spectroscopy

Laser Raman Spectroscopy is a non-destructive diagnostic technique used to identify the structure, and hence the purity, of diamond films, without requiring preparation of the sample. The structure of a material is determined by shining a monochromatic light, in the form of a laser, onto the sample and analysing how the light is scattered.[127] Most of the photons undergo an elastic process, Rayleigh scattering, where the scattered light retains the same energy as the incident light. However, a small portion of the photons undergo an inelastic process, Raman scattering, where energy is exchanged through interactions with the vibrational modes of the crystal lattice, resulting in the scattered light shifting in energy.[127] The frequency shifts that correspond to this exchange of energy provides a structural fingerprint of the sample in the form of a Raman spectrum, where each peak in the spectrum corresponds to a specific vibrational mode.

Figure 2.13: Renishaw 2000 laser Raman spectrometer with a green Ar+ laser at a wavelength of 514nm. Implemented to determine presence of diamond and its purity. Image from[128].

Laser Raman spectroscopy provides rapid, high-resolution data that can be readily interpretated. It is a particularly useful technique for characterisation of diamond films, as pure diamond has a distinct, sharp peak at 1332 cm^{-1}, corresponding to its sp^3 hybridised carbon bonding.[129] In CVD-grown diamond, non-diamond carbon phases may also be present in the sample, such as amorphous carbon or graphitic carbon which has distinctive bands located at approximately 1355 cm^{-1} (D band) and 1575 cm^{-1} (G band).[130] The relative intensities of these features vary depending on the degree of disorder in the crystalline structure of the diamond.

For this project, the Renishaw 2000 laser Raman spectrometer (Figure 2.13), possessing a green Ar+ laser at a wavelength of 514 nm, was used to acquire Raman spectra. Before any

measurements were taken, the spectrometer was calibrated using a piece of single-crystal diamond. Acquisitions were taken with the following conditions: Either 5 accumulations at 3 s of laser exposure and a power of 33%, or 5 accumulations, at 5 s of laser exposure and power of 50%, depending on the quality of the signal retrieved.

2.3.2 LEXT Laser Microscope

The During the project, the Olympus LEXT OLS5100 laser microscope (Figure 2.14) was used to analyse and capture both 2D and 3D scans of the surface morphology of the diamond-coated substrates. The LEXT implements a confocal optical system by scanning a focused laser of 405 nm across the surface of the sample and only allowing focused light to be reflected through a pinhole aperture.[131]

Figure 2.14: The Olympus LEXT OLS5100 laser microscope. Image taken from[131].

For the diamond-coated Si wafers, the surface topography of the substrate was analysed to characterise the roughness of the sample at the submicron level and hence give an indication about the influence on the adhesive properties of the wafer. Additionally, the thickness of the diamond coating on the tungsten fibres was calculated using the height profile analysis available on the LEXT data analysis software. 3D profiles of each substrate coated in CVD diamond were produced to assess the diamond growth, but in particular the diamond-coated fibres, to enable comparison between the hot filament reactor and the Thomas Swan reactor. The LEXT enabled data acquisitions to be performed without sample preparation, over a magnification range of 10-100x and allowed immediate analysis of the 3D scans retrieved, making this a convenient and highly accurate method of characterisation.

2.3.3 Scanning Electron Microscopy

Scanning electron microscopy is a characterisation technique used to analyse the surface morphology of a sample via high-resolution imaging. Although SEM only provides details on the

appearance of the sample surface, in conjunction with Raman Spectroscopy to determine the material's structural fingerprint, it is a very powerful tool.

During the SEM imaging process, a beam of electrons is generated through thermionic emission from a W filament and accelerated via an external voltage. Under high vacuum conditions, this beam is focused onto the sample via a system of electromagnetic lenses. The beam is scanned across the surface and signals from backscattered and secondary electrons caused by interactions between the electron beam and the sample surface are detected, generating images of the surface.[132]

For this project, all substrates were imaged using the JEOL IT300 scanning electron microscope (Figure 2.15) with varying magnifications, working distances in the range of 9.4 – 11.2 mm and a probe current of either 20 or 30 A. The beam energy was set to 20 kV for all wire imaging but was reduced to 15 kV for some of the diamond-coated Si wafer images. The parameters for the SEM were decided based on image clarity.

Figure 2.15: On the left, the full JEOL IT300 scanning electron microscope set-up and the computer to control the electron beam inside the chamber and capture images accordingly. On the right, inside the chamber, where the sample is inserted and held under vacuum.

3. Results and Discussion

3.1 Fabrication of 10 x 10 mm Diamond-Coated Silicon Wafers

3.1.1 Raman Spectroscopy Analysis

After calibration with a piece of single-crystal diamond, the Renishaw 2000 laser Raman spectrometer was utilised to verify the composition of the diamond film deposited on the 10 x 10 mm Si wafer. In the Raman spectrum depicted in Figure 3.1, a sharp first-order peak can be identified at 1332 cm^{-1}, consistent with the characteristic diamond peak extensively reported in literature.[129, 130] The broad band identified adjacent to the diamond peak can be attributed to the presence of non-diamond carbon phases in the form of graphitic or amorphous carbon, often found at the grain boundaries.[133] The characteristic features of sp^2-bonded carbon are reported in literature as the G-band (~1580 cm^{-1}), arising from stretching of sp^2 bond pairs, and the 'D-band' (~1350 cm^{-1}), arising from the 'breathing mode', radial expanding and contracting of carbon atoms, simulating a likeness to breathing, hence the name.[134]

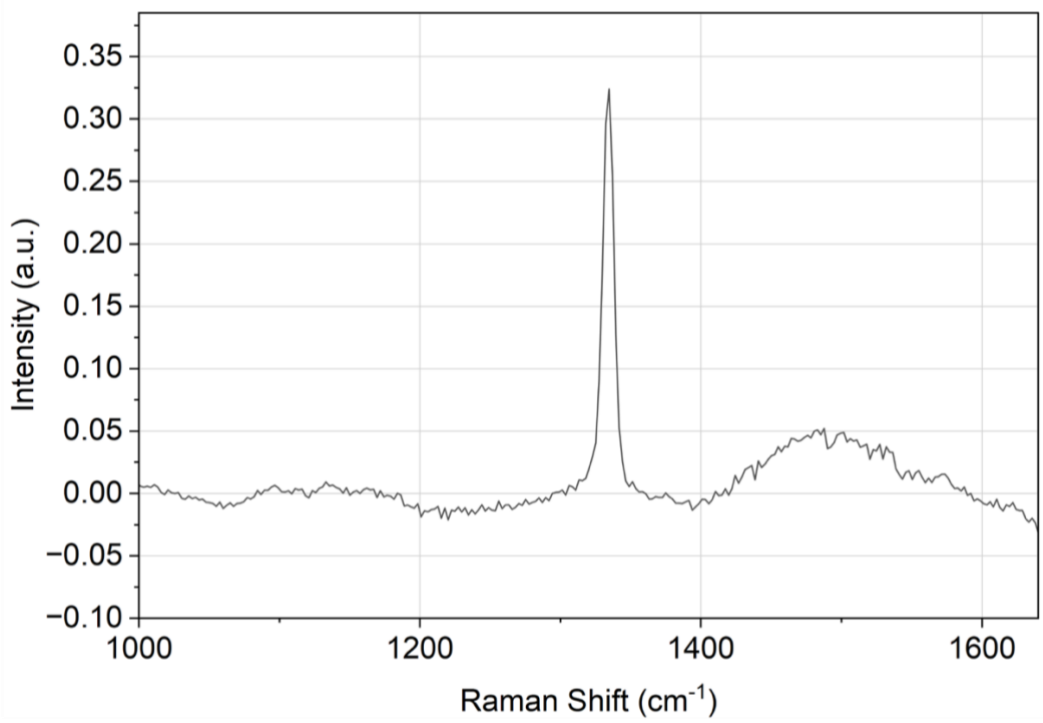

Figure 3.1: Raman spectrum of diamond-coated Si wafer taken at 514 nm. A baseline reduction was performed to remove the rising background to account for background signal due to photoluminescence.

In Figure 3.1, the D- and G-bands are not distinct, indicating that any sp^2 carbon present is highly disordered and lacks long-range structure.[133] Instead, a weak band is observed across 1400-1600 cm^{-1}, resulting from the broadening of the G- and D-bands as the sp^2 character becomes more disordered and the (ordered) graphite peak at 1580 cm^{-1} shifts downwards.[133] Relative to the diamond peak, the amorphous carbon feature is indistinct and low in intensity, implying a low concentration of sp^2-bonded carbon and therefore a high purity of sp^3 bonded diamond. It has been well established that a smaller FWHM of the diamond peak, corresponds to a higher quality of diamond. A FWHM of (8.07 ± 0.58) cm^{-1} from the diamond peak indicates high diamond purity when compared to literature values[111, 135].

3.1.2 Surface Analysis using SEM and LEXT Imaging Techniques

3.1.2.1 LEXT imaging

The 3D acquisition tool on the Olympus LEXT was implemented to give an indication of the roughness of the diamond surface on the Si wafer through a 3D height visualisation, as seen in Figure 3.2. The height colour scale illustrates the distribution of asperities apparent on the surface by showing the variation in the surface height. This was also confirmed by an axial slice measurement of the wafer to create a roughness profile, as seen in Figure 3.2, depicting how the surface topology fluctuates. An appropriate rugosity enhances interfacial adhesion by increasing the surface area available and providing the opportunity for mechanical interlocking with a polymer matrix.[136] Surface roughness measurements obtained from the LEXT analysis demonstrated an average roughness (Ra) of 0.067 µm and an RMS roughness (Rq) of 0.085 µm. Despite these values being on such a micro-scale, L.A. Thimons et. al, reported that the length range of topography that has the most significant impact on macroscopic adhesion for CVD diamond surfaces is between 43 nm – 1.8 µm.[137] Additionally, a maximum peak height (Rp) of 0.337 µm indicates the presence of surface asperities, further contributing to surface roughness for adhesion. These inhomogeneities in the surface are utilised by the liquid polymer to spread across the substrate surface more easily. If the polymer chosen naturally wets the diamond surface, an increase in the surface roughness will reduce the contact angle formed at the surface interface of the diamond-polymer, improving the wettability.[138]

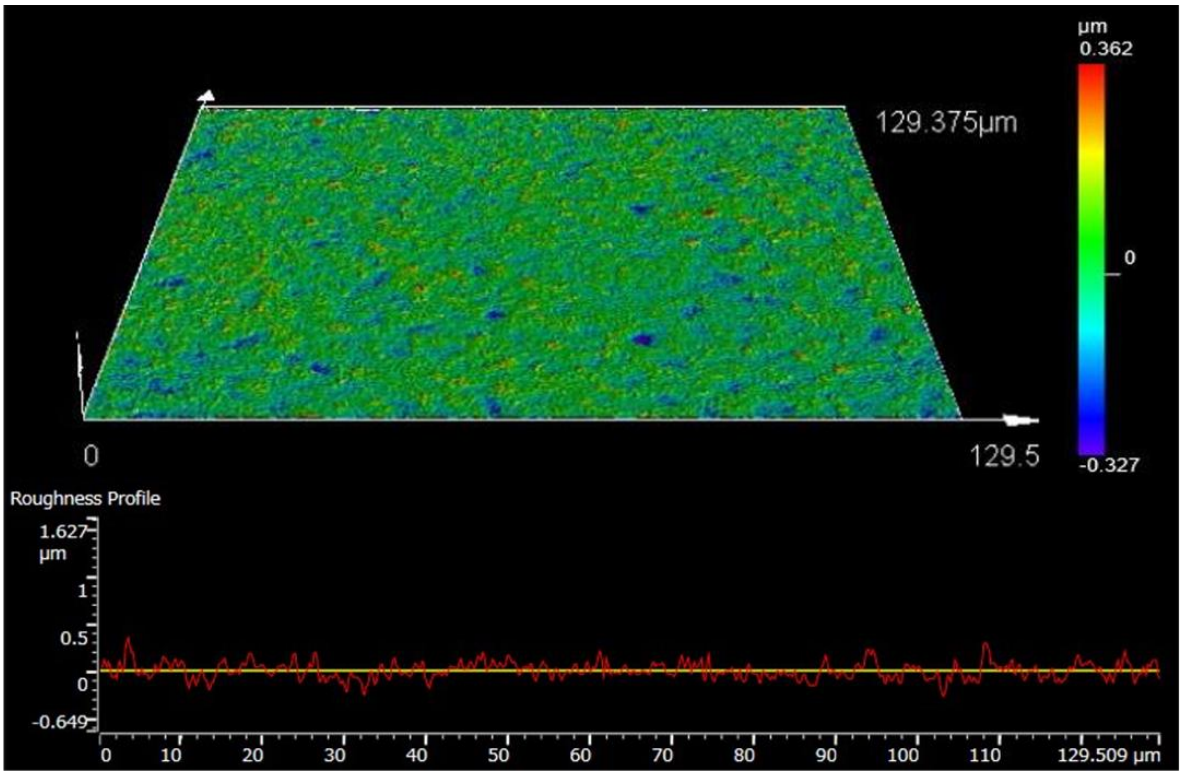

Figure 3.2: On top, a LEXT 3D scan of the diamond-coated Si wafer. Blue areas correspond to surface valleys and red areas correspond to surface peaks. Underneath, the roughness profile depicting the fluctuations in the roughness.

The thickness of the diamond growth on the wafer was calculated using the LEXT 3D acquisition tool. A clean 10 x10 mm Si wafer (without diamond coating) and one of the 10 x10 mm diamond-coated Si wafers were placed next to each other, on top of a spare silicone piece and the height difference was calculated. Once the sample had been noise- and tilt-corrected, a height profile was taken, illustrated in Figure 3.3, giving a height difference, and hence a diamond thickness of 6.56 µm. This corresponds to a growth rate of 1.09 µm h^{-1}, which was as expected for a growth in the HF reactor.

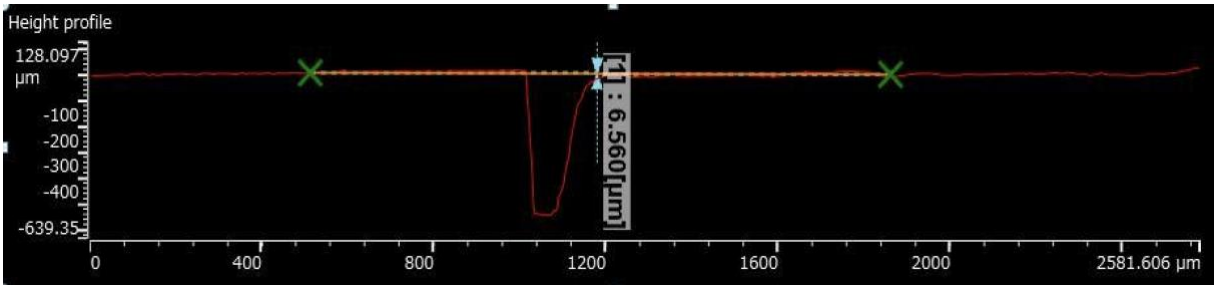

Figure 3.3: Height profile of the Si wafer coated in diamond to determine diamond thickness.

3.1.2.2 SEM Imaging

The SEM was used to obtain images of the diamond-coated Si wafer surface, to assess the surface morphologies prior to adhesion testing. It can be seen in Figure 3.4 that polycrystalline CVD diamond successfully covered the Si wafer, with the surface dominated by smaller micro-scale crystals, but interspersed with larger grain sizes. Mixed morphologies of <111> and <110> can also be identified from Figure 3.4, specifically in Figure 3.4D.

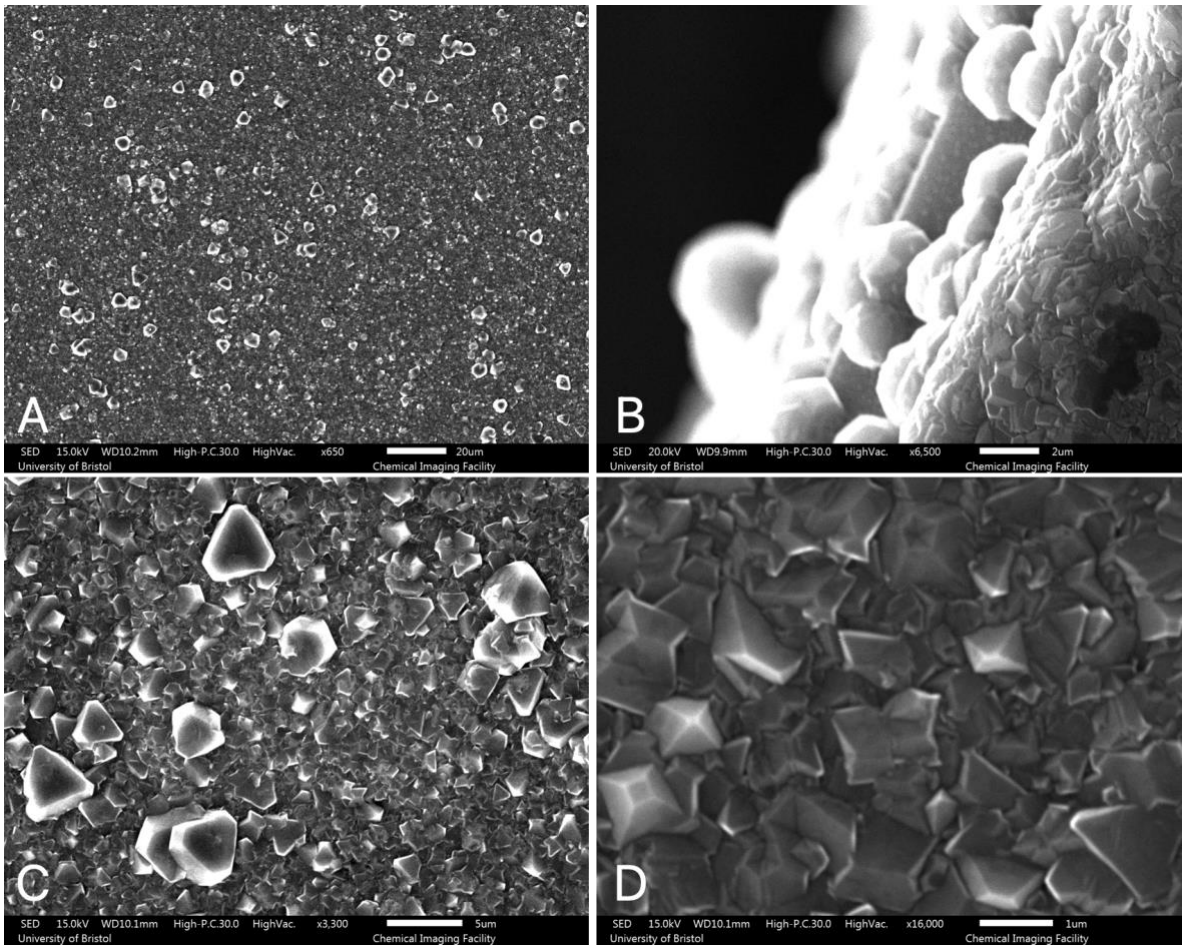

Figure 3.4: SEM images obtained of the 10 x 10 mm diamond-coated Si wafers, all taken with a probe current of 30 A. A) Illustrates the dominance of smaller micro-level grains sizes interspersed with larger grains at x650 magnification B) The edge of the Si wafer with deposited diamond layer at x6500 magnification. C) A closer image of the larger crystal structures and how they form clusters at x3300 magnification. D) Depicts the <111> and <100> crystal structures at x16000 magnification.

The grain size of 100 randomly selected crystals from 3 representative SEM images (Figure 3.4A, 3.4B and 3.4C) were obtained using ImageJ software to measure the Feret diameter. The average grain diameter was determined to be (1.52 ± 0.81) µm, where the error was calculated using the standard deviation of the sample. The error value is relatively large, indicating high variability of the surface due to the inclusion of the larger crystals in the sample area alongside

smaller grains. This variability is likely due to the competing growth and re-nucleation processes that occur during CVD, since the rates of crystal growth, nucleation and growth time directly influence the grain size.[126] The maximum grain diameter from the sample area was determined to be 6.24 μm. It is important to note that grain size increases with film thickness, which is influenced heavily by the growth time, but in this case a growth time of 6 hours was sufficient to produce a consistent and high-quality diamond film for the purpose of adhesion testing.

3.1.3 Initial Adhesion Testing of Diamond-Coated Si Wafer with Selected Polymer

The adhesion testing was done in collaboration with the NCC, including the use of extraction booths for the resin bonding and the use of their specialised pull-off testing equipment. The high Tg resins originally requested for adhesion testing included phthalonitrile, a very thermally stable but brittle thermosetting resin,[139] cyanite ester, a well understood and highly temperature resistant resin, and epoxy, which includes many variants and is easy to process due to its low viscosity. However, some logistical difficulties were encountered which restricted the resin bonding process at the NCC, including no availability in the extraction booths during the allocated timeframe and delays in the approving of COSHH forms and BPSS checks. Therefore, the chosen polymers were limited to commercially available epoxy resins, Bisphenol A compounds.

Table 10: Pull-off force measured via the PosiTest AT-A Automatic Pull-Off Adhesion Tester and pull-off method described in Section 2.2.2. Note, Resin A is Bisphenol A epichlorhydrin ('RS Pro Epoxy Resin') and Resin B is Bis-[4-(2,3-epoxypropoxy) phenyl]propane ('Gorilla Epoxy Resin').

Diamond-Coated Si Wafer Sample	Polymer	Pull-Off Force / N
1	Resin A	**0**
2	Resin B	**9**
3	Resin B	**42**
4	Resin B	**66**

The pull-off force results can be seen in Table 10. Resin A on diamond Sample 1 peeled away with zero applied force, indicating little to no adhesion with the surface. The pull-off force recorded for Sample 2 with Resin B was due to a failure in the bond between the aluminium dolly and the resin, which separated at a force of 9 N, despite the adhesion between the resin and the sample being intact. Therefore, two optimisations were made before the following pull-off tests on Samples 3 and 4 were carried out. Firstly, Resin B was used for *both* samples, and secondly, the surface of the aluminium dolly was roughened using a scouring pad, followed by cleaning with acetone and isopropyl alcohol, to promote adhesion with the resin. Unfortunately, upon transport to the NCC laboratory for testing, Sample 3 was fractured slightly, resulting in a small chip on the corner. This suggests an explanation for the lower pull-off force recorded for

Sample 3 than Sample 4. Although the pull-off forces are not of large magnitude, they clearly demonstrate that the CVD diamond surface will adhere to an epoxy-based resin, which addresses the main objective of the initial adhesion testing. However, it would be beneficial to repeat adhesion testing, as the fracture on Sample 3 leaves only Sample 4 as a reliable result for Resin B.

In addition to the surface roughness of diamond impacting adhesion with the polymer, the surface chemistry at the interface and chemical properties of the polymer resins can also affect adhesion. Immediately after growth, CVD diamond films typically exhibit hydrogen-terminated surfaces, due to the high hydrogen levels present during deposition. Hydrogen-terminated regions, which are non-polar and hydrophobic, result in poor wettability and adhesion with resins, as only weak intermolecular interactions can form.[140] However, exposure to air can lead to partial oxidation, introducing oxygen-containing functional groups that allow adhesion interactions with the resin, despite the chemical inertness of diamond. The measurable force recorded from the pull-off testing results indicate that there were oxygen-containing functional groups present on the surface of the diamond from some degree of oxygen-termination. Nevertheless, there may be inconsistencies in the surface chemistry of each sample. Without the use of further analytical techniques, more specifically X-ray photoelectron spectroscopy (XPS), the degree of surface oxidation that each sample may have undergone during the period of atmospheric exposure cannot be quantified.[141]

Despite both resins having a structure based on the same chemical species, Bisphenol A diglycidyl ether, as the resins were commercially purchased (Resin A as ‘RS Pro Epoxy Resin’ and Resin B as ‘Gorilla Epoxy Resin’), their formulations may differ due to the incorporation of additives or coupling agents. The differences in their commercial formulations lead to variation in adhesion with the diamond surface for each resin. Resin B contains a low viscosity, silane coupling agent, [3-(2,3- epoxypropoxy)propyl]trimethoxysilane, which enables bond formation by acting as a bridge between the diamond surface and the epoxy resin.[142] The silane can interact with the oxygen-containing functional groups present on the diamond surface, whilst integrating into the epoxy matrix, improving the interfacial bonding.[142] In comparison, Resin A does not contain a coupling agent in its formulation, instead relying on weak intermolecular interactions. Additionally, an increased epoxide group availability due to differences in formulation, may influence the adhesion at the interface.

Furthermore, it can be inferred that the viscosities of the resins also differed due to these formulation differences. It is likely that Resin B exhibited a lower viscosity and therefore improved wettability, compared to Resin A, which likely exhibited a higher viscosity, limiting its ability to wet the diamond surface. This may be due to a higher percentage of low molecular weight epoxy groups in Resin B than Resin A.

It should be acknowledged that in reinforcement applications, it is favourable for the diamond fibres to allow for purposeful debonding to ensure that when the composite bends, the fibre can move slightly, reducing composite fracture.[70] However, for thermal management applications such as heat pipes, it is more beneficial for the fibres to be fixed in place to maximise thermal transport, as the composite is being utilised for its thermal conductivity properties rather than its fracture strength. Therefore, in addition to the surface roughness of the diamond wafer, to promote further adhesion at the interface, the surface chemistry can be altered. For example, oxygen-termination introduces polar groups to the hydrophobic surface of diamond, enhancing hydrophilicity and hence, improving wettability and interfacial bonding.[140] Therefore, incorporating an oxygen-termination step, for example oxygen plasma treatment, into the processing of the diamond surfaces would alter the surface chemistry to enhance interfacial bonding, rather than relying on the inconsistent oxidation as a result of exposure to air.

It is also important to note, the PosiTest AT-A Automatic Pull-Off Adhesion Tester is designed for much greater forces than that of the tests performed on the samples in this project, hence the lack of a force response curve. Although this would have provided additional insights into the adhesion behaviour of the resin and diamond surface, these measurements were intended as initial adhesion tests, with the key aim to determine if there was a measurable adhesion between a polymer and the chemically inert diamond surface at all. It should also be considered that the differences in the morphology of the planar, diamond-coated Si wafer compared to the diamond-coated wire, may introduce uncertainty when transferring the adhesion results between the two geometries.

3.2 Fabrication of Diamond-Coated Tungsten Wires in the Hot Filament Reactor

3.2.1 Raman Spectroscopy Analysis

The Raman spectrum obtained for the diamond-coated tungsten wires grown in the HF reactor is depicted in Figure 3.5. The sharp distinct peak seen at 1332 cm^{-1}, confirms the presence of diamond on the sample. The FWHM of (10.32 ± 0.71) cm^{-1}, reflects a sharp peak and indicates the quality of diamond is comparable to that grown on Si.[111] The Raman spectrum in Figure 3.5 is similar to the Raman spectrum for the diamond-coated Si wafer in Section 3.1, however, there is slightly more graphitic character, characterised by the prominent band centred around 1510 cm^{-1}. The graphitic D-band can appear as a 'shoulder' in the spectrum, which can be identified extending from the side of the diamond peak at around 1350 cm^{-1}.[143] It can be inferred that more sp^2 carbon is present than on the Si wafer, resulting in a slightly lower diamond quality in comparison, which is something to be considered when carrying across the adhesion results recorded in Section 3.1 for the fabrication of FRPs.

The observed increase in sp^2 character is likely due to a decrease in grain size, consequently increasing the density of grain boundaries where amorphous carbon mainly resides.[133] In comparison to the planar and manually pre-seeded Si wafers, the radial geometry of the tungsten wire provides a more complex substrate for diamond growth, leading to less control over uniform nucleation and growth. However, the diamond peak is still prominent and sharp in relation to the sp^2 bonding character, indicating a high quality of diamond, which is essential to exploit the properties of diamond when implemented in a composite. The relatively small peak observed at ~1100 cm^{-1} is associated with trans-polyacetylene (TPA) located at grain boundaries, further confirming the presence of non-diamond carbon.[133]

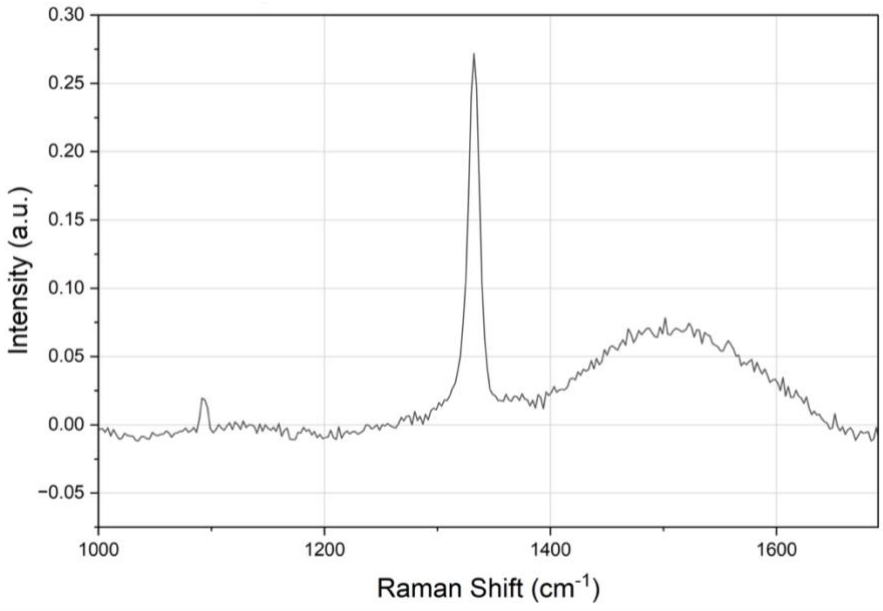

Figure 3.5: Raman spectrum of diamond-coated W wire taken at 514 nm. As previously, a baseline reduction was performed to remove the rising background to account for background signal due to photoluminescence.

3.2.2 Surface Analysis using SEM and LEXT Imaging Techniques

3.2.2.1 LEXT Imaging

The LEXT laser microscope was utilised to retrieve a 3D visualisation of the surface of the diamond-coated wire, to perform an initial assessment of the diamond growth coverage, but primarily to measure the thickness of the growth. By adjusting the 3D acquisition settings on the LEXT software, the scan was taken, ensuring that the full wire was captured. The 3D scan was tilt corrected, the noise was reduced, and a height profile was outputted, as seen in Figure 3.6. As the diameter of the W wire was 100 µm, by taking a horizontal point-to-point of the diameter, the

diamond growth thickness was determined as 5.9 µm. This corresponds to a growth rate of 0.74 µm h^{-1}, which is slower than predicted for the HF reactor.

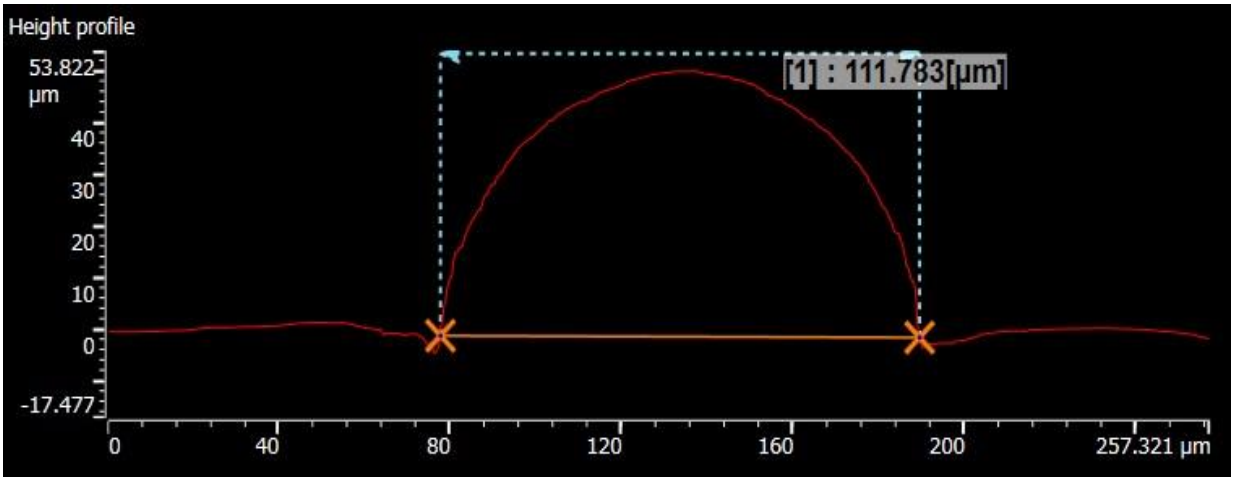

Figure 3.6: The outputted height profile from the 3D acquisition of the diamond-coated wire taken on the LEXT laser microscope. Considering the W wire was 100 µm, the thickness can be calculated to be 5.9 µm.

Additionally, the roughness parameters, Ra and Rq were obtained as 0.479 µm and 0.601 µm respectively, by taking a roughness profile along the direction of the wire. In comparison to the values for the Si wafer, these are much higher, but this can be attributed to the variation in the growth on the wire. The diamond film on the Si wafer is relatively uniform and restricted to a 2D surface, whereas the tungsten wire has non-uniform growth and roughness parameters will particularly be affected by the larger clusters of diamond present in some areas of the wire.

3.2.2.1 SEM Imaging

The SEM images in Figure 3.7 demonstrate an inconsistent and non-uniform growth across the diamond-coated W wires. The HF reactor is optimised for diamond deposition on planar substrates, not irregular or rounded surfaces, such as wires. Therefore, despite positioning each wire slightly raised, underneath and parallel to a filament 3 mm away, the diamond growth was fastest on the sides directly under the filament, limiting uniformity of the coating and resulting in variation in the stages of diamond growth on the wire. Figure 3.7A shows distinct octahedral and cuboid facets characteristic of sp^3 diamond bonding, with the average grain size determined to be (1.13 ± 0.43) µm, using ImageJ software with the same procedure as previously. This section of the wire displays polycrystalline diamond of a relatively consistent grain size and distribution, with the sharper edges of the crystals suggesting a higher degree of order, rather than rounded, amorphous or graphitic carbon heavy films. Similar uniform coating can be seen from a lower magnification in Figure 3.7C on the underside of the wire. However, larger crystals on the top of the wire indicate secondary nucleation or more rapid growth in this area.

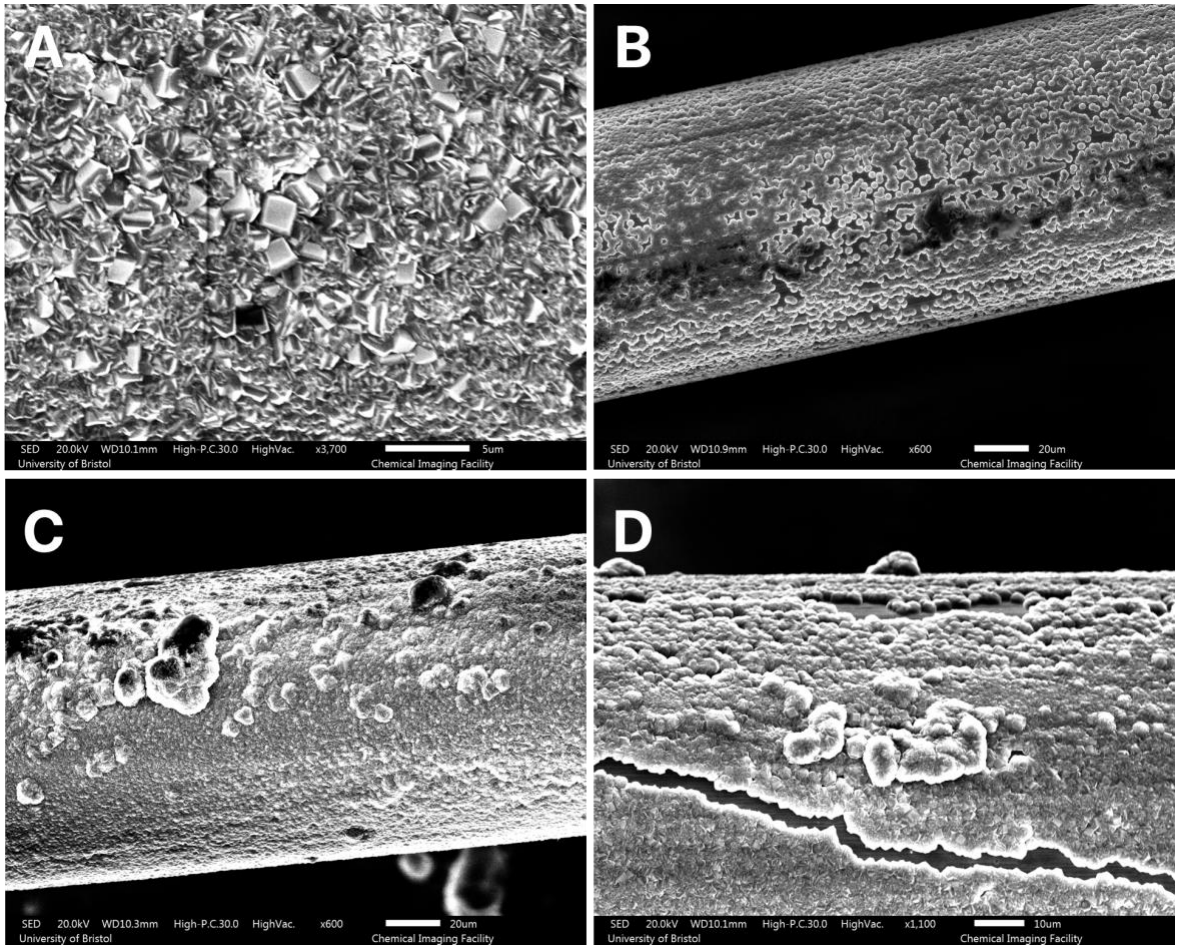

Figure 3.7: Images captured using SEM. A) A section of the wire with polycrystalline diamond growth of relatively consistent grain size and distribution. B) The nucleation stage of the diamond growth. C) Variation in the diamond film, demonstrating the larger clusters. D) Shows a crack running through the diamond film.

The non-uniformity of the diamond growth in the wire is reconfirmed in Figure 3.7B, which illustrates the nucleation stage, consistent with the diamond growth phases (carbide layer followed by diamond nucleation) described in Section 1.5.1.2. Prior to thicker, continuous film formation, these nuclei exhibit similar diameters of (1.98 ± 0.38) μm and regular distribution, and it can be inferred that the carbide layer is beneath these nuclei.[111] The consistency observed in this nucleation stage would predict potential for uniform film if this nucleation had occurred simultaneously across the whole wire. However, this nucleation region is observed amongst other areas of the wire at a different growth stage or with different diamond coverage, such as in Figure 3.7C and D, where large clusters of diamond aggregates of grain height from ~ 3 μm to 25 μm compared to the surrounding ~ 0.5 μm – 1.5 μm crystals can be seen.

The time allocated for the growth was 8 hours, which may not have allowed enough time for continuous film formation on a surface of this geometry, as previously produced diamond-coated tungsten fibres have been under growth conditions for longer, or with an optimised set up to

promote uniform coating, such as positioning the wire substrate inside of the coils of the filament. The larger diameter crystals in Figure 3.7C, present a potential for the thickness of the growth, if the conditions, such as growth time, were optimised.

The lateral cracks present in Figure 3.7D re-confirm the non-uniformity of the coverage. It is possible that it is associated with the difference in coefficient of thermal expansion between the CVD diamond and tungsten. As the wire is cooled after the CVD process, the tungsten may have contracted more than the diamond, creating areas of stress and due to its brittle nature, causing it to break.[111] However, tungsten is typically chosen as a substrate for CVD diamond growth due to its low thermal expansion coefficient.

The images in Figure 3.7 collectively suggest that the wire is in different stages of diamond growth due to local variations in growing conditions, but there is potential that an increased growth duration would have evened out these stages.

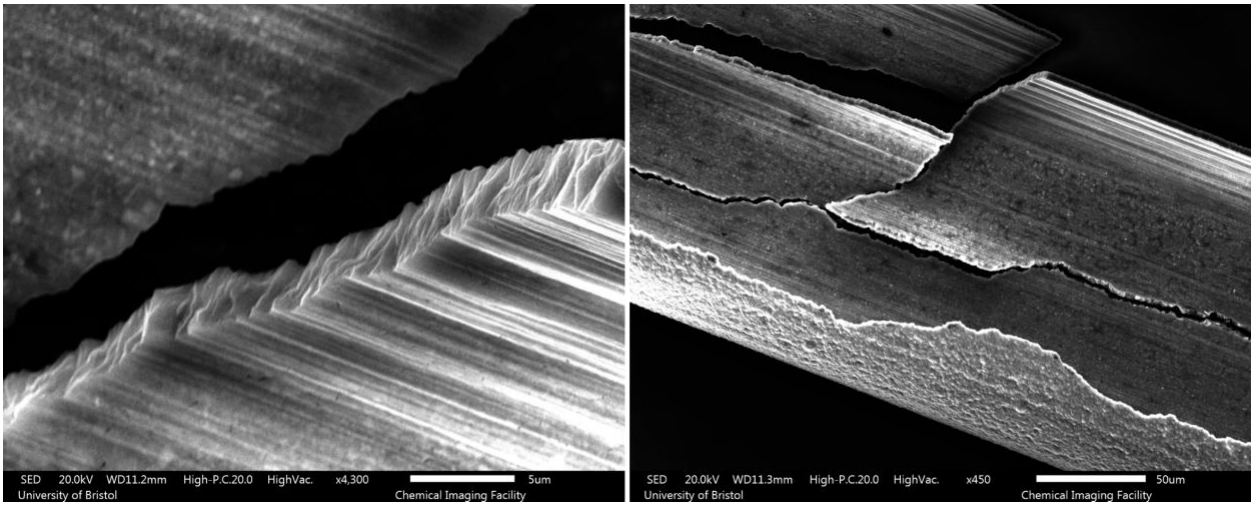

Figure 3.8: The edge of the diamond coating that has broken away from the wire by getting attached to the carbon tape.

Figure 3.8 depicts the diamond coating that separated from the W wire during the SEM process. To load the samples into the SEM chamber for viewing, the samples had to be mounted onto the stubs via carbon tape. However, due to the small size of the three diamond-coated wires, the carbon tape pulled the diamond away from a section of one of the wires upon rearranging. It is likely that this was enabled by the non-uniform coating and would be prevented with a thicker, uniform coated wire. However, the wire imprints can be seen on the inside of the diamond film, indicating that the film adhered well to the surface of tungsten and the initial nucleation phase was successful in specific areas. The thickness of the segment in Figure 3.8 was determined to be 4.2 µm, which differs slightly from the thickness calculated using the LEXT scan, but variation in coating thickness is expected based on the SEM results, especially in this segment as it was thin enough to break away from the wire under the force of the tape.

3.3 Fabrication of Diamond-Coated Tungsten Wires in the Thomas Swan Reactor

The primary purpose of the 8-hour run was to verify the performance of the Thomas Swan reactor after it had been out of use for multiple years. The run demonstrated that the reactor could deposit diamond films successfully to an extent, sustain filament heating and gas flow throughout the process and operate without triggering the interlock system to shut down. The following 20-hour growth performed in three cycles was in replacement of an overnight run, which was not possible as the Thomas Swan reactor could not be left unattended overnight. Although the overnight run would have been able to test the long-term stability of the Thomas Swan reactor in preparation for longer growths, the three cycle growth process instead provided insights into the viability of this method.

3.3.1 Raman Spectra analysis

The Raman spectra obtained for the 8-hour growth (Figure 3.9A) and the 20-hour growth (Figure 3.9B) both illustrate a more prominent non-diamond carbon band than the previous Raman spectra discussed. The diamond peak is still easily distinguishable at 1332 cm^{-1} in both Raman spectra, but is weaker and more broadened, with a FWHM of 19.67 cm^{-1} and 19.64 cm^{-1} respectively, indicating a lower diamond purity than previously. This is reconfirmed by the relative ratios of the sp^3 diamond peak and the sp^2 amorphous or graphitic non-carbon feature. The weak D-band shoulder around 1350 cm^{-1} is not well resolved and overlaps with the G-band feature over 1420 cm^{-1} – 1650 cm^{-1}, indicating the sp^2 phase is highly disordered.

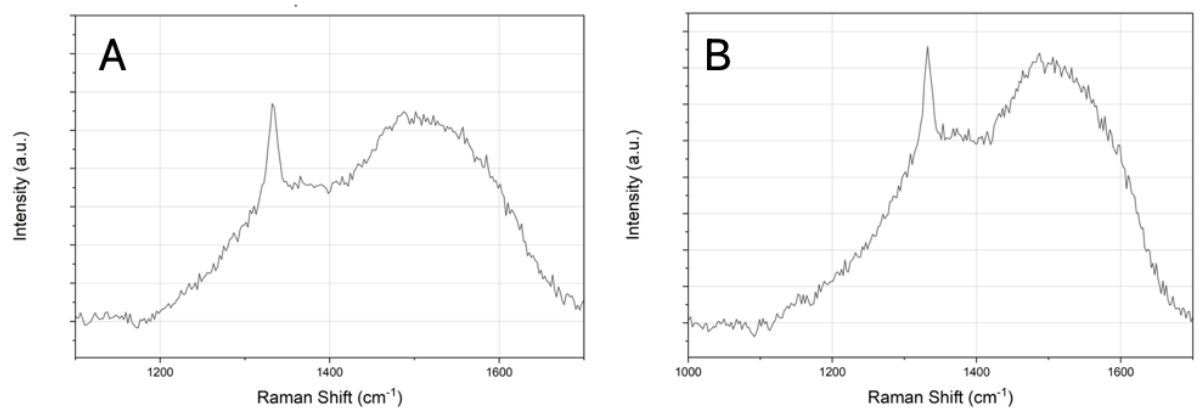

Figure 3.9: Raman spectra of diamond-coated W wire grown in the Thomas Swan taken at 514 nm. A) 8-hour growth B) 20-hour growth. A baseline reduction was performed to remove the rising background to account for background signal due to photoluminescence.

Under continuous growth conditions, with an increased growth time of 20 hours, it would be expected that the diamond purity would improve, but this idea did not transfer across to the

interrupted growth. Instead, the non-diamond carbon phases are higher in intensity for the 20-hour growth, indicating that the three-cycle method did not improve the diamond quality despite the longer total growth time.

When comparing Raman spectra obtained from the different substrates, it is important to consider the differences in the reactor configurations. The HF reactor possesses a smaller chamber appropriate for shorter (8-hour) growths, whereas the Thomas Swan reactor has a much larger chamber, designed for extended periods of growth, up to 72 hours. Therefore, it is likely that the wires produced in the Thomas Swan reactor were at an early stage of their diamond film development when the growth process was stopped, which may explain the low diamond purity observed in the Raman spectrum.

In the case of using wires for strength applications, it is of interest to note that sp^2 carbon phases located at grain boundaries may reduce crack propagation or delamination in diamond films by reducing internal stress, though too much sp^2 character weakens the diamond film structure, reducing hardness and Young's Modulus.[144]

3.3.2 Surface Analysis using SEM and LEXT Imaging Techniques

3.3.2.1 LEXT Imaging

3D scans of the diamond-coated wires grown in the Thomas Swan reactor were acquired, using the same method as previously. Two batches of wires were produced: those grown for 8 hours and those grown for 20 hours in three cycles of 6 – 7-hour growths.

The diamond film thickness for the 8-hour wire was determined to be ~ 5.8 μm, corresponding to a growth rate of 0.725 μm h^{-1}, which falls within the range of predicted growth rate for the Thomas Swan reactor. The 20-hour diamond thickness was determined to be ~ 13.3 μm, corresponding to a growth time of 0.66 μm h^{-1} , which, although is within the predicted range of the Thomas Swan reactor, is slower than the 8-hour growth. Due to the impossibility of an overnight run during the project timeframe, the growth was carried out in three cycles, where between each cycle, the reactor was pumped down to vacuum and the power to the filament stopped, resulting in cooling of the wire. Both the wire substrate and the tungsten filament stayed intact during the cooling and re-heating of the reactor, but the growth was stopped after 20 hours to prevent breakage as the filament was beginning to bend. However, the cooling of the wires after each cycle, meant that the wires had to re-heat at the beginning of the substituent cycle before growth could continue, disrupting columnar growth and introducing repeating nucleation phases, hence decreasing the growth rate. The growth rate is heavily impacted by the temperature of the substrate and the filament and consistency is required.[107] There is limited research into the effects of interrupted CVD growth for extended periods (overnight), apart from studies that remove the substrates from the reactor for short periods of time to take SEM images to track

nucleation and growth.[145] However, a study by J. Lee *et al.* investigated interrupted gas flow during the CVD process which resulted in similar observations of reduced growth rate.[146]

Despite the diamond film being thicker than that of the 8-hour growth, no improvement in the diamond quality was observed, and it remained below the standard of that on the HF wire or the Si wafer. This suggests that the three-cycle growth method was ineffective and not ideal for optimal growth.

The observation of a distinct diamond peak indicates that the reactor is capable of depositing diamond, despite an extended period spent out of use. Additionally, it must be stressed that as this was the first run in the Thomas Swan, the aim was to assess the functionality of the reactor, so the conditions were not exhaustively optimised. In subsequent runs, film quality is expected to improve with longer growth times and refined growth conditions. For example, a decrease in methane concentration has been found to result in larger diamond grain sizes and hence a lower volume of grain boundaries where amorphous carbon resides.[133] Consequently leading to a lower intensity of the amorphous band relative to the diamond peak, indicating a higher quality of diamond growth. Furthermore, it has been established that increasing the density of nucleation sites leads to an increase in growth rate.[107] Therefore, manual pre-seeding of the W wire substrates may have increased initial nucleation site density, prompting improved film uniformity, although, this would potentially be negligible when reaching 30–40-hour growths.

3.3.2.2 SEM Imaging

The SEM was implemented to assess the coverage of the diamond film for the 8-hour growth, however, due to time constraints, it was not possible to execute SEM imaging for the 20-hour growth. This is unfortunate, as it would give a better indication of the coverage, the growth stage and how the interrupted growth method affected the morphology of the diamond.

Figure 3.10 enables a visualisation of the growing stages of diamond film, from early-stage growth to the beginning of continuous film. Figure 3.10A illustrates the nucleation stage and how these isolated diamond spheres begin to merge together to form the continuous film. The isolated spherical clusters are of similar size, with an average diameter of around (7.68 ± 0.61) μm. The surface texture of this continuous diamond film can be seen with a higher magnification in Figure 3.10B, demonstrating densely packed uniform grains, prior to <111> or <100> facet formation. However, upon close inspection, sharper edged, square crystal geometries can be seen starting to form. This small grain size corresponds to a high grain boundary density, which rationalises the high sp^2 content in the Raman spectra.

Figure 3.10C demonstrates clear lateral cracking along the direction of the wire. This could be due to the difference in the thermal expansion coefficients causing stress, or due to the brittleness of the diamond film due to the limited thickness. A lower magnification image of the wire in

Figure 3.10D has been included to provide a clearer perspective of how the diamond coating sits relative to the wire and larger diamond grains can be seen beginning to form on certain areas of the wire. The missing coating (the coating gap) on the left underside of the W wire is likely due to the coating breaking away when the wire was cut to fit into the SEM chamber for viewing. Figures 3.10C and D were used to determine an average film thickness of (5.01 ± 0.63) µm using ImageJ software, which is in agreement with the value determined on the LEXT.

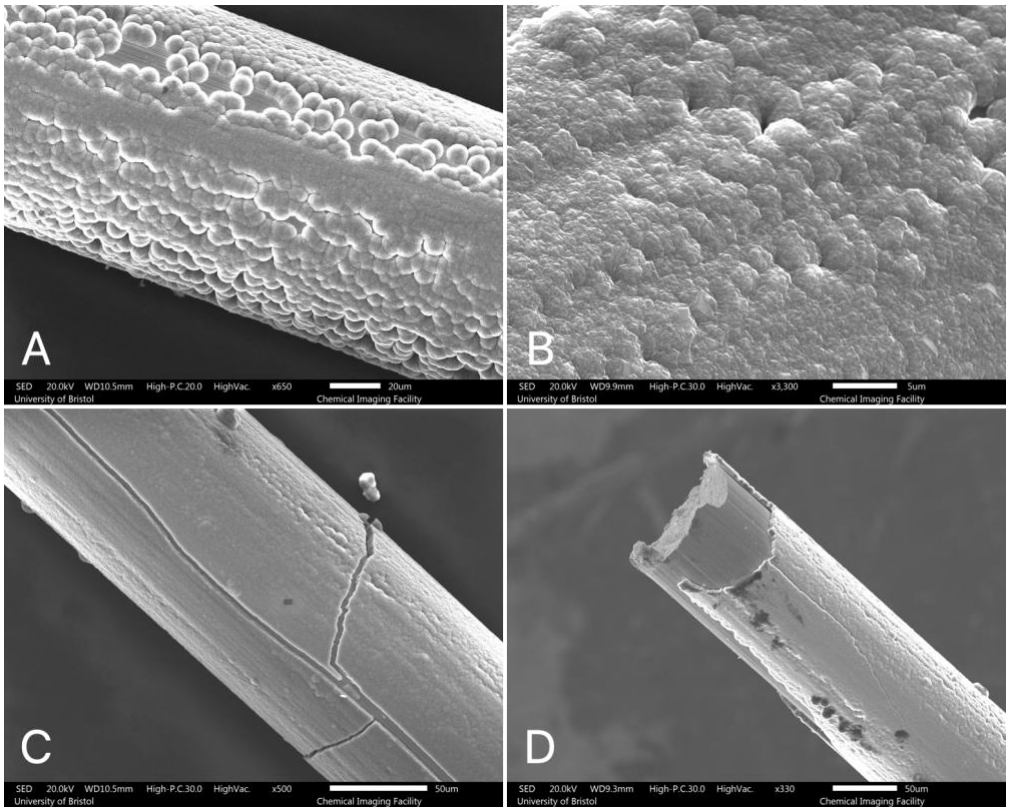

Figure 3.10: SEM images taken with a probe current of 20 or 30 A and 20 kV. A) Nucleation phase of the diamond formation, illustrated by spherical diamond clusters. B) The start of continuous diamond film formation. Small, closely packed grains and a high density of grain boundaries agree with the sp^2 content in the Raman spectra. C) Cracks in continuous diamond coating. D) Lower magnification of the diamond wire showing the film on the wire.

Overall, Figure 3.10 confirms the immature growth of the wire in the Thomas Swan reactor and indicates that a longer growth time was needed. Previous studies on diamond-coated W wires have shown that the quality of diamond increases nearer to the top of the film, where the grain size is larger and the density of grain boundaries is smaller with increasing thickness.[121] From this, it can be insinuated that the diamond quality would increase with longer growth time and therefore, thickness.

3.3.2.3 Aside on Grain Size

It has been demonstrated that the thermal conductivity of the diamond film is heavily dependent on the grain morphology. As established, as the grain sizes in a CVD diamond film get larger, there is decrease in grain boundary density and defects present, which act as scattering sites for phonons, disrupting the thermal transport system.[121] Thermal conductivity measurements of up to 900 W m^{-1} K^{-1} have been reported for CVD diamond fibres.[121] Furthermore, when these diamond fibres were embedded in epoxy to create composites, high efficiency of thermal conductivity was displayed.[121] Therefore, it would be beneficial to prioritise an improvement in grain size, via the optimisation of CH_4 concentration and temperature, if the diamond-coated wires were to be used in thermal management applications. However, it can be inferred that the diamond-coated wires grown in both the HF reactor and the Thomas Swan reactor were in early-stage growth, so larger grain size would naturally follow with film thickness.

In the case of strength applications, it should be noted that diamond fibre strength had a negative correlation with coating thickness and hence grain size, especially in films growth at a high growth rate and high methane concentrations.[144] Additionally, Young's modulus is heavily affected by grain size dependent on methane concentration implemented during the growth.[144]

4. Conclusions

Polycrystalline CVD diamond was successfully deposited on six 10 x 10 mm Si wafers, forming a relatively uniform coating and a higher diamond quality than the diamond-coated wires produced in both the HF reactor and the Thomas Swan reactor. This is likely due to the planar, pre-seeded substrate suited for the well-established growth method in the HF reactor. In comparison, the HF process was not optimised for the geometry of the wire, and the Thomas Swan growth was primarily a trial run without optimised conditions.

The adhesion testing performed was preliminary and intended to assess the viability of adhesion between a polymer resin and the chemically inert diamond surface. The pull-off force results provide evidence of measurable adhesion between the CVD diamond surface and a commercially available Bisphenol A epoxy formulation containing a silane coupling agent. Additionally, these adhesion results suggest presence of oxygen-containing functional groups on the diamond surface due to natural oxidation when exposed to atmosphere but require further XPS verification.

The diamond-coating on the wires grown in the HF reactor was of high purity and comparable to that of the diamond film on the Si wafer. However, the growth was inconsistent, with variable thickness across the three wires, denoting the different stages of growth. Although longer growth times or optimisation of conditions should be investigated, the current results are advantageous in enabling visualisation of the different stages of diamond growth.

Diamond-coated tungsten wires were fabricated through the HFCVD process in the Thomas Swan reactor, confirming the overall aim of repurposing and reactivating the reactor. However, the Raman spectrum of these diamond wires illustrated high sp^2 content with a lower diamond purity than the two other methods of production. It is apparent from the SEM images that the diamond wires produced as a result of the 8-hour run in the Thomas Swan reactor were in the early-stages of growth, providing justification for this Raman data. The diamond wires produced using the three-cycle method were of poorer quality than all previously produced wires, despite exhibiting a thicker diamond coating. This indicates that even with a longer total growth duration, this method was ineffective likely due to the repeated heating and cooling of the wire, disrupting continuous diamond growth.

With optimisation of growth conditions, the thickness and quality of the diamond coating have potential to improve, resulting in stiffer and stronger diamond fibres with high thermal conductivity. These fibres can be implemented into diamond fibre reinforced polymers for structural or thermal management applications. The development of high-performance diamond FRPs offers a lightweight, remarkably strong, thermally conductive composite, effectively harnessing the exceptional qualities of diamond.

5. Future work

The key priority for future work regarding operation of the Thomas Swan reactor would include optimising the conditions for CVD diamond growth through variation of CH_4:H_2 ratio, substrate and filament temperature and growth time. For thermal management applications, increasing the grain size of the diamond films through these optimisations would be beneficial, particularly by varying methane concentration. For the possibility of longer uninterrupted runs, a hydrogen generator will need to be implemented to the Thomas Swan reactor set-up, as consistent H_2 is essential for overnight growth.

It would be advantageous to test the fibre-matrix adhesion properties with further polymers, including phthalonitrile and cyanite ester, to assess the need for roughness control or surface functionalisation, such as oxygen termination. Additionally, the use of XPS can quantify not only the degree of oxygen coverage on the surface, but also can determine the presence of different oxygen species, providing more insight on the surface chemistry of the samples.[141]

Incorporating these diamond fibres into a polymer matrix for the fabrication of diamond FRPs is the crucial next step, followed by the testing of mechanical and thermal performance and investigation into failure mechanisms, such as interfacial adhesion and fibre pull-out or fracture.

6. References

1. T.-D. Ngo, in *Composite and Nanocomposite Materials - From Knowledge to Industrial Applications*, ed. T.-D. Ngo, IntechOpen, London, 2020.
2. D. Hull and T. W. Clyne, *An Introduction to Composite Materials*, Cambridge University Press, Cambridge, 2 edn., 1996.
3. J. Bai, in *Advanced Fiber-Reinforced Polymer(FRP) Composites for Structural Applications (Second Edition)*, ed. J. Bai, Woodhead Publishing, 2023, pp. 93-99.
4. S. Maiti, M. R. Islam, M. A. Uddin, S. Afroj, S. J. Eichhorn and N. Karim, *Advanced Sustainable Systems*, 2022, **6**, 2200258.
5. C. Nemessányi, *Periodica Polytechnica Architecture*, 2023, **54**, 193-206.
6. B. Parkyn, *Glass Reinforced Plastics*, Butterworth & Co (Publishers) Ltd, London, 1970.
7. B. De, M. Bera, D. Bhattacharjee, B. C. Ray and S. Mukherjee, *Progress in Materials Science*, 2024, **146**, 101326.
8. W. Han, J. Zhou and Q. Shi, *Alexandria Engineering Journal*, 2023, **64**, 541-579.
9. M. S. Murad, A. K. Hamzat, E. Asmatulu and R. Asmatulu, *Advanced Composites and Hybrid Materials*, 2024, **8**, 31.
10. I. O. Oladele, V. O. Oki, T. F. Omotosho, M. B. Adebanjo, O. T. Ayanleye and S. A. Adekola, *Next Materials*, 2025, **8**, 100775.
11. K. Malik, F. Ahmad, E. Gunister, T. Nakato, E. Mouri, M. Muhammad and S. Ali, *Journal of Natural Fibers*, 2021, **19**, 1-25.
12. M. A. M. Rizal, M. Yahya, S. Hassan, I. R.A, D. Chin, N. Mas'ood, W. Abdul Saad, A. Yusop and M. Rafidah, 2023, **2**, 1-16.
13. N. Gebremedhin and G. Rotich, *International Journal of Polymer Science*, 2020, **2020**, 1-9.
14. P. Jayaraman, A. Pai, M. Rodriguez-Millan, S. Shenoy B, C. K N and S. Hegde, *Materials Research Express*, 2024, **11**, 015508.
15. R. Rahman and S. Zhafer Firdaus Syed Putra, in *Mechanical and Physical Testing of Biocomposites, Fibre-Reinforced Composites and Hybrid Composites*, eds. M. Jawaid, M. Thariq and N. Saba, Woodhead Publishing, 2019, pp. 81-102.
16. M. M. Alzahrani, K. A. Alamry and M. A. Hussein, *Results in Chemistry*, 2025, **15**, 102199.
17. G. O. Edah, J. O. Atiba and O. S. I. Fayomi, *Next Materials*, 2025, **8**, 100743.
18. M. C. Ribeiro, A. Fiúza, A. Ferreira, M. D. Dinis, A. C. Meira Castro, J. P. Meixedo and M. R. Alvim, *Recycling*, 2016, **1**, 178-193.
19. J. Qureshi, *Sustainability*, 2022, **14**, 16855.
20. S. A. Mirdehghan, in *Engineered Polymeric Fibrous Materials*, ed. M. Latifi, Woodhead Publishing, 2021, pp. 1-58.
21. J. Zangenberg and P. Brøndsted, in *Fatigue of Textile Composites*, eds. V. Carvelli and S. V. Lomov, Woodhead Publishing, 2015, pp. 403-440.
22. E. Alrehaili, A. Nurdiawati and S. G. Al-Ghamdi, *Resources, Conservation & Recycling Advances*, 2025, **28**, 200294.
23. F. Aramide, P. Atanda and O. Olorunniwo, *International Journal of Composite Materials*, 2012, **2**, 147-151.

24. C. Călin, A. Diniță, G. Brănoiu, D. R. Popovici, M. Tănase, E.-E. Sirbu, A.-I. Portoacă and S. Mihai, *Polymers*, 2024, **16**, 1779.
25. F. G. Alabtah, E. Mahdi and M. Khraisheh, *Materials*, 2021, **14**, 6501.
26. G. D. Sims and W. R. Broughton, in *Comprehensive Composite Materials*, eds. A. Kelly and C. Zweben, Pergamon, Oxford, 2000, pp. 151-197.
27. D. K. Rajak, P. H. Wagh and E. Linul, *Polymers*, 2021, **13**, 3721.
28. I. Shakir Abbood, S. a. Odaa, K. F. Hasan and M. A. Jasim, *Materials Today: Proceedings*, 2021, **43**, 1003-1008.
29. J. Li, R. Zhao, Y. Wang, Y. Chen, X. Kong and B. Du, *Composite Structures*, 2023, **318**, 117083.
30. S. Li, H.-H. Tsang, Y. Cheng and Z. Lu, *Composite Structures*, 2018, **194**, 454-467.
31. S. Waghmare, S. Shelare, K. Aglawe and P. Khope, *Materials Today: Proceedings*, 2022, **54**, 682-689.
32. MatWeb, Overview of Properties for D-Glass Fiber, https://www.matweb.com/search/DataSheet.aspx?MatGUID=3984c45fd4a449dfbfa4909d2a9060df, (accessed February 2026).
33. T. Sathishkumar, S. Satheeshkumar and J. Naveen, *Journal of Reinforced Plastics and Composites*, 2014, **33**, 1258-1275.
34. T. Ramakrishnan, M. D. Mohan Gift, S. Chitradevi, R. Jegan, P. S. Hency Jose, H. N. Nagaraja, R. Sharma, P. Selvakumar and S. M. Hailegiorgis, *Advances in Materials Science and Engineering*, 2022, **2022**, 1088926.
35. X. Huang, *Materials*, 2009, **2**, 2369-2403.
36. D. D. L. Chung, in *Carbon Fiber Composites*, ed. D. D. L. Chung, Butterworth-Heinemann, Boston, 1994, pp. 3-11.
37. T. Harano, Y. Takeichi, M. Usui, Y. Arai, R. Murao, N. Negi and M. Kimura, *Applied Sciences*, 2020, **10**, 4836.
38. J. Qureshi, *Fibers*, 2022, **10**, 27.
39. M. Davidson, R. Graunke, A. Green, H. Haelsig, L. Heinemann, S. Antony Jose and P. L. Menezes, *Fibers*, 2026, **14**, 29.
40. A. Krzyzak, E. Kosicka, M. Borowiec and R. Szczepaniak, *Materials*, 2020, **13**, 1364.
41. D. S. Vijayan, A. Sivasuriyan, P. Devarajan, A. Stefańska, Ł. Wodzyński and E. Koda, *Buildings*, 2023, **13**, 1509.
42. M. Vaughan, A. Beaucamp and M. N. Collins, *Composites Part B: Engineering*, 2025, **292**, 112024.
43. Q. Mao, S. Rajabpour, M. K. Talkhoncheh, J. Zhu, M. Kowalik and A. C. T. van Duin, *Nanoscale*, 2022, **14**, 6357-6372.
44. S. Dabees, L. C. Henderson and D. J. Hayne, *Composites Part B: Engineering*, 2025, **306**, 112758.
45. R. Fan, T. Yan, J. Su, H. Zhao, L. Zha, J. Zhou and S. Zhu, *Journal of Macromolecular Science, Part A*, 2023, **60**, 29-37.
46. Y.-t. Liu, L. Li, J.-p. Wang, Y.-j. Fei, N.-d. Liu and G.-p. Wu, *New Carbon Materials*, 2021, **36**, 639-648.
47. G. Zhang, S. Sun, D. Yang, J.-P. Dodelet and E. Sacher, *Carbon*, 2008, **46**, 196-205.
48. M. Zhang, X. Qian, K. Ma, H. Ma and Y. Zhang, *Applied Composite Materials*, 2022, **29**, 745-764.

49. B. Wang, Y. Duan, J. Zhang and X. Zhao, *Composites Part B: Engineering*, 2016, **99**, 398-406.
50. Z. Xu, L. Chen, B. Zhou, Y. Li, B. Li, J. Niu, M. Shan, Q. Guo, Z. Wang and X. Qian, *RSC Advances*, 2013, **3**, 10579-10597.
51. M. Ertekin, in *Fiber Technology for Fiber-Reinforced Composites*, eds. M. Ö. Seydibeyoğlu, A. K. Mohanty and M. Misra, Woodhead Publishing, 2017, pp. 153-167.
52. X. Xu, Y. Guo, Z. Shen, B. Liu, F. Yan and N. Zhong, *Polymers*, 2025, **17**, 2254.
53. J. W. S. Hearle, in *Handbook of Textile Fibre Structure*, eds. S. J. Eichhorn, J. W. S. Hearle, M. Jaffe and T. Kikutani, Woodhead Publishing, 2009, vol. 2, pp. 450-457.
54. A. He, T. Xing, Z. Liang, Y. Luo, Y. Zhang, M. Wang, Z. Huang, J. Bai, L. Wu, Z. Shi, H. Zuo, W. Zhang, F. Chen and W. Xu, *Advanced Fiber Materials*, 2023, **6**, 3-35.
55. A. He, T. Xing, Z. Shi, Y. Zhang, Y. Luo, M. Wang, Z. Huang, S. Qiao, A. Tong, S. Chen, F. Chen and W. Xu, *Materials & Design*, 2024, **242**, 112989.
56. A. Engelbrecht-Wiggans, F. Burni, E. Guigues, S. Jiang, T. Huynh, Z. Tsinas, D. Jacobs and A. Forster, *Textile Research Journal*, 2020, **90**, 2428-2440.
57. T. Xu, Z. Qi, Q. Yin, Y. Jiao, L. An and Y. Tan, *Polymers*, 2022, **14**, 4892.
58. J. Nasser, J. Lin, K. Steinke and H. A. Sodano, *Composites Science and Technology*, 2019, **174**, 125-133.
59. I. Elfaleh, F. Abbassi, M. Habibi, F. Ahmad, M. Guedri, M. Nasri and C. Garnier, *Results in Engineering*, 2023, **19**, 101271.
60. M. Syduzzaman, M. A. Al Faruque, K. Bilisik and M. Naebe, *Coatings*, 2020, **10**, 973.
61. P. Peças, H. Carvalho, H. Salman and M. Leite, *Journal of Composites Science*, 2018, **2**, 66.
62. V. Lakshmi Narayana and L. Bhaskara Rao, *Materials Today: Proceedings*, 2021, **44**, 1988-1994.
63. M. George, P. Mussone, K. Alemaskin, M. Chae, J. Wolodko and D. Bressler, *Journal of Materials Science*, 2016, **51**, 2677-2686.
64. V. Koutsos, *Adhesives*, 2025, **1**, 11.
65. M. M. Mohammed, M. Rasidi, A. M. Mohammed, R. B. Rahman, A. F. Osman, T. Adam, B. O. Betar and O. S. Dahham, *BioResources*, 2022, **17**, 7031-7090.
66. V. Dhinakaran, M. D. Vijayakumar, G. Muthu, T. Sathish and P. M. Bupathi ram, *Materials Today: Proceedings*, 2021, **37**, 1799-1803.
67. T. Lih, A. Azmi and N. Muhammad, *Advanced Materials Research*, 2014, **980**, 8-12.
68. H. Junaedi and T. A. Sebaey, *Journal of Physics: Conference Series*, 2024, **2805**, 012008.
69. M. Ö. Seydibeyoğlu, A. Dogru, J. Wang, M. Rencheck, Y. Han, L. Wang, E. A. Seydibeyoğlu, X. Zhao, K. Ong, J. A. Shatkin, S. Shams Es-haghi, S. Bhandari, S. Ozcan and D. J. Gardner, *Polymers*, 2023, **15**, 984.
70. S.-J. Park and M.-K. Seo, in *Interface Science and Technology*, eds. S.-J. Park and M.-K. Seo, Elsevier, 2011, vol. 18, pp. 501-629.
71. I. Shyha and D. Huo, *Advances in Machining of Composite Materials Conventional and Non-conventional Processes: Conventional and Non-conventional Processes*, Springer, Switzerland, 2021.
72. Corrosionpedia, Glass Transition Temperature (Tg), https://www.corrosionpedia.com/definition/593/glass-transition-temperature-tg, (accessed April 2026).
73. S. Anwar and X. Li, *Journal of Coatings Technology and Research*, 2024, **21**, 461-480.

74. N. Saba, M. Jawaid, O. Y. Alothman, M. Paridah and A. Hassan, *Journal of Reinforced Plastics and Composites*, 2016, **35**, 447-470.
75. A. D. Almutairi, *Polymers*, 2024, **16**, 3185.
76. C. Sonnenfeld, H. Mendil-Jakani, R. Agogué, P. Nunez and P. Beauchêne, *Composite Structures*, 2017, **171**, 298-305.
77. J. W. Kim and J. S. Lee, *Materials*, 2016, **9**, 448.
78. R. Ece, F. Ozturk and M. Çobanoğlu, *Journal of Thermoplastic Composite Materials*, 2023, **0(0)**, 1-33.
79. T. Koottatep, in *Marine Plastics Abatement : Technology, Management, Business and Future Trends* 2023, vol. 2, pp. 285-310.
80. S. Lazăr, D. Dobrotă, R.-E. Breaz and S.-G. Racz, *Polymers*, 2023, **15**, 3634.
81. I. McKay, J. Vargas, L. Yang and R. M. Felfel, *Materials*, 2024, **17**, 4878.
82. H. Moulya, *Journal of Engineering and Applied Science*, 2026, **73**, 82.
83. N. Sathiya Narayanan, D. Sai Venkat Mohan, J. Abhinay, T. Dinesh, V. Satya Sai Surya Teja and R. Praneeth, *Scientific Reports*, 2024, **14**, 27524.
84. M. E. Annadorai, M. Ramakrishna and Y. Jyothi, *Interactions*, 2024, **245**, 198.
85. Y. S. Mohamed and A. Abdelbary, *Alexandria Engineering Journal*, 2023, **67**, 693-705.
86. D. G. Raghavendra, P. Naidu, S. Ojha, Vasavi, M. Panchal and s. K. Acharya, *Materials Research Express*, 2019, **6**, 115353.
87. C. Lewis, B. O. Yavuz, M. L. Longana, J. P. H. Belnoue, K. R. Ramakrishnan, C. Ward and I. Hamerton, *Journal of Composites Science*, 2024, **8**, 318.
88. P. Mallick, *Fiber-Reinforced Composites*, CRC Press, Florida, USA, 3 edn., 2007.
89. M. Y. Zaghloul and M. M. Y. Zaghloul, *Polymers (Basel)*, 2022, **14**, 2662.
90. M. Ahmad Sawpan, K. Pickering and A. Fernyhough, *Journal of Composite Materials*, 2013, **47**, 1513-1525.
91. D. G. Lee and S. S. Cheon, *Journal of Composite Materials*, 2001, **35**, 27-56.
92. J. Qiao, Q. Zhang, C. Wu, G. Wu and L. Li, *Polymers*, 2022, **14**, 3080.
93. T. L. Price, G. Dalley, P. C. McCullough and L. Choquette, *Handbook: Manufacturing Advanced Composite Components for Airframes*, U. S. D. o. T. Federal Aviation Administration Report DOT/FAA/AR-96/75, Office of Aviation Research, Washington, D. C., 1997.
94. V. Volpe, S. Lanzillo, G. Affinita, B. Villacci, I. Macchiarolo and R. Pantani, *Polymers*, 2019, **11**, 326.
95. Y.-M. Chen and J.-M. Ting, *Carbon*, 2002, **40**, 359-362.
96. D. K. Rajak, D. D. Pagar, P. L. Menezes and E. Linul, *Polymers (Basel)*, 2019, **11**, 1667.
97. M. Mehdikhani, L. Gorbatikh, I. Verpoest and S. V. Lomov, *Journal of Composite Materials*, 2019, **53**, 1579-1669.
98. A. Diniță, R. G. Ripeanu, C. N. Ilincă, D. Cursaru, D. Matei, R. I. Naim, M. Tănase and A. I. Portoacă, *Polymers*, 2024, **16**, 2.
99. G. Sumithra, R. N. Reddy, G. Dheeraj Kumar, S. Ojha, G. Jayachandra and G. Raghavendra, *Materials Today: Proceedings*, 2023, https://doi.org/10.1016/j.matpr.2023.1004.1637.
100. A. P. Mouritz, in *Introduction to Aerospace Materials*, ed. A. P. Mouritz, Woodhead Publishing, 2012, pp. 303-337.
101. P. May, *Philosophical Transactions of the Royal Society of London. Series A: Mathematical, Physical and Engineering Sciences*, 2000, **358**, 473-495.

102. P. W. May, The Molecule of the Month, Diamond, https://www.chm.bris.ac.uk/motm/diamond/diamondh.htm, (accessed March, 2026).
103. S. Tennant, in *Philosophical Transactions of the Royal Society of London*, 1797, vol. 87, ch. 4, pp. 123-127.
104. F. P. Bundy, H. T. Hall, H. M. Strong and R. H. Wentorfjun, *Nature*, 1955, **176**, 51-55.
105. W. G. Eversole, *United States Pat.,* 3030187; 3030188, 1958.
106. B. V. Deryagin, D. V. Fedoseev, V. M. Lukyanovich, B. V. Spitsyn, A. V. Ryanov and A. V. Lavrentyev, *Journal of Crystal Growth*, 1968, **2**, 380.
107. S. Zhou, Z. Zhihao, X. Ning and Z. Xiaofeng, *Materials Science and Engineering: B*, 1994, **25**, 47-52.
108. M. Uddin, K. H. W. Seah, L. Xiaoping, M. Rahman and K. Liu, *Wear*, 2004, **257**, 751-759.
109. K. W. Chae and Y. J. Baik, *Diamond and Related Materials*, 1999, **8**, 1261-1266.
110. E. D. Nicholson, J. R. Weeks and M. N. R. Ashfold, *Diamond and Related Materials*, 1997, **6**, 817-821.
111. M. D. Whitfield, J. A. Savage and R. B. Jackman, *Diamond and Related Materials*, 2000, **9**, 262-268.
112. P. W. May, C. A. Rego, R. M. Thomas, M. N. R. Ashfold, K. N. Rosser and N. M. Everitt, *Diamond and Related Materials*, 1994, **3**, 810-813.
113. J. L. Davidson and X. Cao, in *Proc. 2nd Int. Symp. on 'Diamond Materials',* Washington D.C., USA, 1991.pp 333-339
114. P. W. May, C. A. Rego, R. M. Thomas, M. N. R. Ashfold, K. N. Rosser, P. G. Partridge and N. M. Everitt, *Journal of Materials Science Letters*, 1994, **13**, 247-249.
115. P. W. May, C. A. Rego, R. M. Thomas, M. N. R. Ashfold, K. N. Rosser, P. G. Partridge and N. M. Everitt, presented in part at the *Proc. 3rd Int. Symp. Diamond Mater*., Honolulu, Hawaii, 1993
116. P. W. May, C. A. Rego, M. N. R. Ashfold, K. N. Rosser, G. Lu, T. D. Walsh, L. Holt, N. M. Everitt and P. G. Partridge, *Diamond and Related Materials*, 1995, **4**, 794-797.
117. J. Ting and M. L. Lake, *Journal of Materials Research*, 1994, **9**, 636-642.
118. J. O. Orwa, J. Reiner, A. Juma, A. Stacey, K. Sears, J. A. Schütz, A. Merenda, L. Hyde, R. Guijt, V. R. Adineh, Q. Li, M. Naebe, A. Z. Kouzani and L. F. Dumée, *Diamond and Related Materials*, 2021, **115**, 108349.
119. L. Ma, L. Zhang, P. Zhao, N. Hu, Z. Gong, W. Ye, Q. Wei, K. Zhou, Z. Yu and Y. Zhang, *Materials & Design*, 2016, **101**, 109-116.
120. J. E. Graebner, *International Journal of Thermophysics*, 1998, **19**, 511-523.
121. P. W. May, R. Portman and K. N. Rosser, *Diamond & Related Materials*, 2005, **14**, 598 - 603.
122. P. W. May, M. Hall and D. J. Smith, *International Journal of Modern Physics B*, 2002, **16**, 906-911.
123. D. Dickes, S. Maidl, J. Riesch, R. Neu and K. Drechsler, *Journal of Composites Science*, 2025, **9**, 161.
124. G. Meaden, P. G. Partridge, E. Nicholson, J. Nicholson, A. Wisbey and M. N. R. Ashfold, *Diamond and Related Materials*, 1997, **6**, 898-901.
125. G. Meaden, P. G. Partridge, M. N. R. Ashfold, E. D. Nicholson and A. Wisbey, *Diamond and Related Materials*, 1996, **5**, 825-828.

126. P. W. May and Y. A. Mankelevich, *The Journal of Physical Chemistry C*, 2008, **112**, 12432-12441.
127. R. R. Jones, D. C. Hooper, L. Zhang, D. Wolverson and V. K. Valev, *Nanoscale Research Letters*, 2019, **14**, 231.
128. U. o. B. C. D. Group, Diamond Characterisation Equipment, https://www.chm.bris.ac.uk/pt/diamond/characterisation.htm, (accessed April 2026).
129. S. A. Solin and A. K. Ramdas, *Physical Review B*, 1970, **1**, 1687-1698.
130. J. Filik, *Spectroscopy Europe*, 2005, **17**, 10-17.
131. EVIDENT, LEXT OLS5100 Laser Microscope, https://evidentscientific.com/en/products/digital-imaging/lext-ols5100, (accessed April 2026).
132. J. Webb and J. H. Holgate, in *Encyclopedia of Food Sciences and Nutrition (Second Edition)*, ed. B. Caballero, Academic Press, Oxford, 2003, pp. 3922-3928.
133. A. Dychalska, P. Popielarski, W. Franków, K. Fabisiak, K. Paprocki and M. Szybowicz, *Materials Science-Poland*, 2015, **33**, 799-805.
134. A. C. Ferrari and J. Robertson, *Philos Trans A Math Phys Eng Sci*, 2004, **362**, 2477-2512.
135. K. Fabisiak, M. Szreiber, C. Uniszkiewicz, T. Runka and D. Kasprowicz, *Crystal Research and Technology*, 2010, **45**, 167-172.
136. A. N. Gent and C. W. Lin, *The Journal of Adhesion*, 1990, **32**, 113-125.
137. L. A. Thimons, A. Gujrati, A. Sanner, L. Pastewka and T. D. B. Jacobs, *Experimental Mechanics*, 2021, **61**, 1109-1120.
138. A. J. Kinloch, *Journal of Materials Science*, 1980, **15**, 2141-2166.
139. B. Han, Y. Li, J. Wan, W. Hu, Q. Chu, Y. Shi, L. Yang and Z. Hu, *Reactive and Functional Polymers*, 2025, **214**, 106293.
140. M. C. Salvadori, W. W. R. Araújo, F. S. Teixeira, M. Cattani, A. Pasquarelli, E. M. Oks and I. G. Brown, *Diamond and Related Materials*, 2010, **19**, 324-328.
141. R. Zulkharnay, G. Zulpukarova and P. May, *Applied Surface Science*, 2024, **658**, 159776.
142. Y. Xie, C. A. S. Hill, Z. Xiao, H. Militz and C. Mai, *Composites Part A: Applied Science and Manufacturing*, 2010, **41**, 806-819.
143. R. Tu, T. Xu, D. Li, S. Zhang, M. Yang, Q. Li, L. Zhang, T. Shimada, T. Goto and J. Shi, *RSC Adv*, 2018, **8**, 16061-16068.
144. E. Kalaugher, N. M. Everitt and E. D. Nicholson, *Diamond and Related Materials*, 1997, **6**, 826-829.
145. K. Kobashi, K. Nishimura, Y. Kawate and T. Horiuchi, *Physical Review B*, 1988, **38**, 4067-4084.
146. J. J. Lee, S. F. Komarov, J. B. Hudson, E. B. Stokes and M. P. D'Evelyn, *Diamond and Related Materials*, 1997, **6**, 511-515.